A Novel Continuous Control Set Current-Based Model Predictive Control for a Three-Phase, Two-Level AC/DC Converter With the LCL Filter

Krzysztof Dmitruk and Andrzej Sikorski

***Abstract*—This article presents a developed novel continuous control set current-based model predictive control (CCS C-BMPC) for an ac–dc grid converter connected to the grid through an *LCL* filter. Most CCS MPC algorithms control the converter current by regulating the reference voltage derived from the prediction algorithm in the final control stage. The proposed algorithm enables direct control of the grid current by regulating the converter current and the voltage on the filter capacitor. The algorithm uses optimized prediction to compensate for the grid current vector error, minimizing total harmonic distortion (THD) at a relatively low switching frequency. It exhibits high robustness to power grid disturbances and avoids current distortions during zero crossing, especially at low current amplitudes. The advantages of the proposed method have been confirmed in simulations and laboratory tests in steady-state and transient conditions. It confirms that the developed control technique shows a high quality of the grid current (low THDi value), high dynamic performance, and immunity in case of weak grid conditions. The proposed method was compared with a method that uses a typical proportional-resonant current controller.**

***Index Terms*—Continuous control set model predictive control (CCS MPC), current control, grid tied inverter, *LCL* filter, pulsewidth modulation, voltage source converter.**

I. Introduction

THE ac–dc converters, connecting dc voltage with the power grid, have become one of the most commonly used power electronic devices. Their popularity has increased primarily due to their application in every converter linking renewable energy sources to the grid [1], [2], [3], [4] and in every electric vehicle charger powered from the grid. Additionally, they find various applications in power supply systems [5], [6] and electric drives. ac–dc voltage converters are typically connected to the power grid using one of two types of passive filters: first-order *L* filter or third-order *LCL* filter. The *LCL* filter provides a higher harmonic damping level than the *L* filter [7]. This reduces the required total inductance values, lowering the converter's cost and dimensions. On the other hand, the *LCL* filter generates a resonant frequency that needs to be attenuated.

All mentioned applications of the ac–dc converter require bidirectional energy flow, sinusoidal current (low grid current total harmonic distortion (THD)), controlled power factor, and low fluctuations in dc-link voltage. The system must be robust to changes in network parameters, converter filter parameters, and disturbances in the power grid. The primary control strategy for ac–dc converters, commonly applied in practice, is voltage-oriented control. It involves indirectly controlling reactive and active power flow through the active and reactive components of currents in a closed-loop regulation system using PI controllers [8], [9]. The controller output signal (converter's set voltage) is reproduced in the space vector modulation (SVM) modulator or three-phase pulsewidth modulation (PWM). Higher control accuracy can be achieved using resonant controllers [10], [11]. Controllers with modulators provide a constant switching frequency (defined harmonic spectrum), facilitating the selection of *L* or *LCL* and electromagnetic interference (EMI) filters parameters. However, this requires selecting controller parameters, negatively impacting set current values tracking in transient states. Additionally, control methods based on PWM/SVM modulators require the application of dead-time correction, whose complexity affects correction quality.

The second group of ac–dc converter control methods is termed nonlinear. One of the oldest strategies is the direct power control (DPC) method, created by analogy to the direct torque control drive method. In the DPC method, active and reactive power control exchanged with the grid is managed without an internal current control loop, using a power comparator-controlled switching table [9], [10], [11] or in the linear version DPC-SVM [12]. With the increase in the computational power of control processors, model predictive control (MPC) became possible [13], [14] in the version with a continuous control set (CCS-MPC) [15], [16], [17], [18], [19], [20] and a finite control set (FCS-MPC) [13], [21].

In the CCS-MPC algorithms, the simplest representative is the deadbeat algorithm [22]. Its control voltage ensures the

Received 22 July 2024; revised 2 October 2024; accepted 11 October 2024. Date of publication 23 October 2024; date of current version 30 June 2025. This work was supported by project WZ/WE-IA/6/2023 of the Bialystok University of Technology and financed from a subsidy provided by the Polish Ministry of Science and Higher Education. Recommended for publication by Associate Editor M. Liserre. *(Corresponding author: Krzysztof Dmitruk.)*

The authors are with the Bialystok University of Technology, 15-351 Bialystok, Poland (e-mail: k.dmitruk@pb.edu.pl; a.sikorski@pb.edu.pl).

Color versions of one or more figures in this article are available at https://doi.org/10.1109/TPEL.2024.3485229.

Digital Object Identifier 10.1109/TPEL.2024.3485229

realization of a specific cost function determined by the converter model and its power supply. Subsequently, this control voltage is reproduced in the converter using PWM/SVM modulation. This modulation implementation ensures a constant switching frequency on the one hand and errors resulting from dead-time on the other hand. These algorithms combine the advantages of linear and nonlinear control systems, maintaining good characteristics in both steady and transient states. The literature also considers using CCS-MPC methods not only for sinusoidal linear loads but also for nonlinear three-phase and single-phase loads in a four-wire power system [23]. The *LC* output filter ensures a sinusoidal power supply with no more than 4% THD voltage under unbalanced load conditions in a steady state, and the system is resistant to 50% changes in *LC* parameters and abrupt load changes. In the article [24], on controlling an ac–dc converter with an *LCL* filter, an adaptive CCS-MPC was additionally designed to resist changes in grid inductance, which can shift the resonance frequency of the *LCL* filter and cause system instability.

The FCS-MPC method utilizes the discrete nature of converters, characterized by a limited number of switching states, to predict the behavior of controlled variables. Calculations are performed at each sampling for all combination connections. The optimal converter voltage vector is selected by minimizing a specified cost function *J*. An extension of this method includes algorithms with additional virtual voltage vectors [25], [26], [27], which significantly reduce current THD by increasing the number of voltage vectors to choose from. Another step in improving current THD is the control method with floating voltage vectors [28]. Instead of many permanently defined virtual vectors, an environment with three virtual vectors for the specified voltage vector has been proposed, allowing the minimization of current THD with significant robustness to changes in the system model parameters. An interesting and forward-looking direction for developing predictive control methods is implementing control with a longer prediction horizon (several to even dozens of steps ahead) when determining the control action in the next step. Such control reduces current THD by several times when extending the prediction horizon to 20 steps and does not require additional measures to dampen resonances (such as active damping) while maintaining a low switching frequency, as shown in publications on three-level drive converters [29], [30]. Moreover, using such a control method demands significant computational effort, growing exponentially with the number of steps, and requires a fast processor or reduced sampling frequency. A smart branch and bound technique called sphere decoding was adopted to efficiently solve the underlying optimization problem computationally in real-time. The long horizon method is effective in steady-state conditions in FCS-MPC methods, where in each step, we only aim to minimize the error of the controlled quantities due to the finite number of available voltage vectors. On the other hand, the principle of CCS-MPC control is to achieve zero error, e.g., of the reference voltage at the end of the control period in each step, by using an "infinite" number of voltage vectors obtained through modulation, e.g., SVM. This excludes the possibility of long-horizon control.

The proposed control method differs from most CCS-MPC methods, where the final stage of control implementation involves determining the reference voltage for the converter, which is then reproduced by the modulator. This necessitates compensating for dead-times and other errors associated with reproducing the desired currents. We directly shape the current in the proposed method, eliminating the intermediate voltage shaping and associated drawbacks. By shaping the current using the CCS-MPC method, we aim to achieve zero current error at each step, correcting the error in the subsequent step. The proposed method involves shaping the converter current to produce a voltage on the filter capacitor similar to the voltage present in the power grid, ensuring a sinusoidal active current drawn from the grid. Directly shaping the converter current involves determining modulation times based on geometric relationships derived from the current vector derivatives for specific voltage vectors. Transient states associated with step changes in the reference value are mapped without modulation, using voltage vectors that achieve the new reference current value in the quickest possible manner. The current change dynamics are limited only by the object's parameters and are characteristic of nonlinear controls, such as deadbeat control or FCS-MPC.

Summarizing the overview of control methods, an input *LCL* filter is a desirable feature of the ac–dc converters. Such a filter introduces additional resonant frequencies, usually requiring additional damping systems (e.g., resistors and active dumping). Additionally, desired characteristics of the ac–dc converter include a low grid current THD, a fixed switching frequency enabling easy construction of EMI filters and selection of *LCL* filter parameters, and mitigation of dead-time issues. These properties were fulfilled in the control system presented in this article.

The rest of this article is organized as follows. Section II introduces the ac–dc converter model with an *LCL* filter. Section III focuses on predictive control using FCS-MPC for grid current regulation in the ac–dc converter. Section IV describes the proposed continuous control set current-based model predictive control (CCS C-BMPC). Subsequently, Sections V and VI present simulation results and compare the proposed method with the Proportional-Resonant (PR) controller. Section VII checks the system's stability when the system model's parameters are detuned from the real parameters. Section VIII presents experimental studies in steady, transient, and voltage disturbance states. Finally, Section IX concludes this article.

II. AC–DC Converter Model

Depending on the selected configuration of conducting transistors, the voltage at the *UVW* terminals [see Fig. 1(a)] can be described in the stationary $\alpha\beta$ reference frame as follows:

$$\boldsymbol{u}_{2\alpha\beta} = \begin{cases} \frac{2}{3}U_{\mathrm{dc}}e^{j(n-1)\frac{\pi}{3}} & : \text{for } n = \{1,2,3,4,5,6\} \\ \prime 0\prime & : \text{for } n = \{7,8\}\,. \end{cases} \tag{1}$$

Fig. 1(b) graphically presents the representation of all output voltage vectors $\boldsymbol{u}_{2\alpha\beta}$ of the converter, described by the above equation.

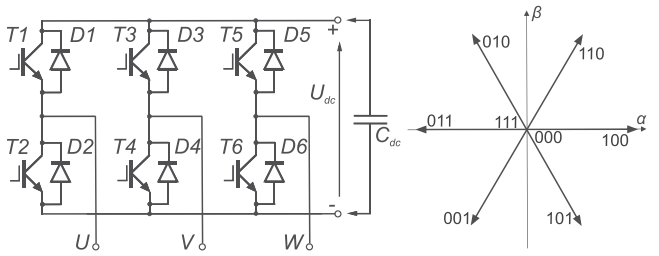

(a) (b)

Fig. 1. (a) Schematic of voltage converter. (b) Available voltage vectors in a stationary reference frame $\alpha\beta$.

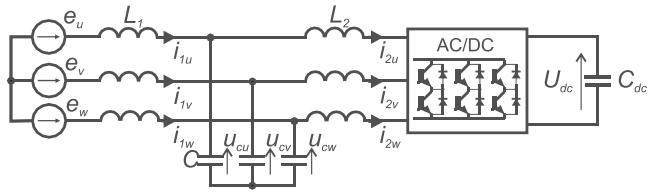

Fig. 2. Scheme of an AC–DC converter with an *LCL*-type passive filter.

An example of using an *LCL*-type passive filter as an interface between the power supply network and the voltage converter is shown in Fig. 2.

Two resonance circuits can be distinguished by analyzing the above schematic of the converter connected to the power grid through an *LCL* filter. The first consists of elements L_1 and C, and the second consists of L_2 and C. To achieve high-quality regulation, appropriate resonance frequency values should be ensured during the filter design stage, avoiding amplifying harmonics generated by the ac–dc converter due to switching frequency. Filter parameter selection should provide high damping of harmonics related to the transistor switching frequency and low damping in the frequency band associated with the fundamental grid current harmonic. Consequently, using an *LCL* filter in the converter-based system significantly complicates the application of nonlinear control methods characterized by variable switching frequencies. Therefore, this article presents a new method, CCS C-BMPC, to control the ac–dc converter. This method uses PWM modulation to minimize higher harmonics introduced into the power grid. Applying modulation of multiple voltage vectors in one control period T_s allows achieving an infinite number of voltage vectors at the ac converter terminals. This means that the resultant voltage vector reproduced by the converter within one control period T_s can be positioned at any point inside the hexagon defined by the vertices of the active vectors of the two-level converter. The primary control principle is to control the voltage on the *LCL* filter capacitor to reflect the shape of the power grid voltage. Assuming a constant inductance value of L_1, fulfilling this principle leads to a sinusoidal grid current. This article demonstrates the possibility of determining three switching times of three ac–dc converter vectors within one control period, T_s, enabling precise control of the voltage on the *LCL* filter capacitor. This is achieved by minimizing the control error of the L_2 inductance current for single T_s as close to zero as possible. Additionally, the modulator generates a constant switching frequency, making filtering unwanted current components through the grid filter easier.

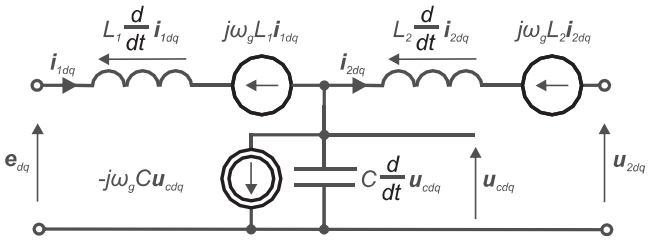

Fig. 3. Scheme of the *LCL* filter in the rotating *dq* reference frame.

A. *Mathematical Model of an* LCL*-Type Passive Filter*

LCL filters consist of inductors on the grid side (L_1), inductors on the converter side (L_2), and filtering capacitors (C) (as shown in Fig. 2). In the stationary $\alpha\beta$ coordinate system, the following equations describe the above system:

$$L_1 \frac{d}{dt} \boldsymbol{i}_{1\alpha\beta} = \boldsymbol{e}_{\alpha\beta} - \boldsymbol{u}_{c\,\alpha\beta} \tag{2}$$

$$L_2 \frac{d}{dt} \boldsymbol{i}_{2\alpha\beta} = \boldsymbol{u}_{c\,\alpha\beta} - \boldsymbol{u}_{2\,\alpha\beta} \tag{3}$$

$$C \frac{d}{dt} \boldsymbol{u}_{c\,\alpha\beta} = \boldsymbol{i}_{1\alpha\beta} - \boldsymbol{i}_{2\alpha\beta} \tag{4}$$

where

$\boldsymbol{e}_{\alpha\beta}$ - grid voltage vector in the stationary $\alpha\beta$ reference frame,
$\boldsymbol{i}_{1\alpha\beta}$ - grid current vector in the stationary $\alpha\beta$ reference frame,
$\boldsymbol{i}_{2\alpha\beta}$ - converter current vector in the stationary $\alpha\beta$ reference frame,
$\boldsymbol{u}_{c\alpha\beta}$ - capacitor filter voltage vector in the stationary $\alpha\beta$ reference frame,
$\boldsymbol{u}_{2\alpha\beta}$ - converter voltage vector in the stationary $\alpha\beta$ reference frame,
L_1 - inductance of the grid side inductor,
L_2 - inductance of the converter side inductor,
C - capacitance of the LCL filter capacitor.

Transferring (2), (3), and (4) to the *dq* reference frame rotating with the grid pulsation ω_g results in the following:

$$L_1 \frac{d}{dt} \boldsymbol{i}_{1dq} = \boldsymbol{e}_{dq} - j\omega_g L_1 \boldsymbol{i}_{1dq} - \boldsymbol{u}_{cdq} \tag{5}$$

$$L_2 \frac{d}{dt} \boldsymbol{i}_{2dq} = \boldsymbol{u}_{cdq} - j\omega_g L_2 \boldsymbol{i}_{2dq} - \boldsymbol{u}_{2dq} \tag{6}$$

$$C \frac{d}{dt} \boldsymbol{u}_{cdq} = \boldsymbol{i}_{1dq} - \boldsymbol{i}_{2dq} - j\omega_g C \boldsymbol{u}_{cdq}. \tag{7}$$

The equivalent scheme of the *LCL* filter in the rotating *dq* reference frame with grid pulsation ω_g is presented in Fig. 3.

III. Description of the FCS-MPC Control Method

FCS-MPC with a cost function involving only one variable, the grid current vector, was utilized for the proposed solution's

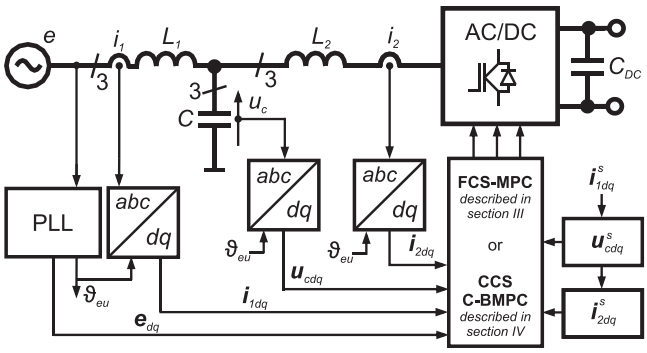

Fig. 4. Block diagram of the control structure.

initial analysis. All operations related to computing successive iterations of the converter control algorithm are performed in a rotating dq reference frame with pulsation ω_g, oriented to the grid voltage vector $\boldsymbol{e}_{dq}$ aligned with the d-axis. The block diagram of the control structure is illustrated in Fig. 4.

The current $\boldsymbol{i}_{2dq}$ flowing in the inductance L_2 is shaped by the voltage difference $\boldsymbol{u}_{cdq}$ on the filtering capacitor C and the voltage $\boldsymbol{u}_{2dq}$ generated by the ac–dc converter at its ac terminals. The voltage at the converter terminals has high dynamic changes (rectangular-shaped voltage) compared to the voltage on the filtering capacitor C. Based on this, it is assumed that the rapidly changing voltage $\boldsymbol{u}_{2dq}$ significantly influences the variations in the current $\boldsymbol{i}_{2dq}$ flowing in the inductance L_2. Using the description of available vectors at the converter ac terminals and the equation describing the loop of the LCL filter circuit from the converter side (6), the vector $\boldsymbol{d}_{2u}$ can be determined. This vector is proportional to the derivative of $\boldsymbol{i}_{2dq}$, indicating the current vector's direction and rate of change

$$L_2 \frac{d}{dt}\boldsymbol{i}_{2dq} = \boldsymbol{u}^*_{2dq} - \boldsymbol{u}_{2dq} = \boldsymbol{d}_{2u}. \tag{8}$$

The vector $\boldsymbol{u}^*_{2dq}$ in (8) is calculated using $\boldsymbol{e}_{dq}$, and voltage drops across the filter inductances. This is expressed by (9) considering sinusoidal waveforms of all quantities, i.e., their fundamental harmonics (marked with an asterisk)

$$\boldsymbol{u}^*_{2dq} = \boldsymbol{e}^*_{dq} - \boldsymbol{i}^*_{1dq} j\omega_g L_1 - \boldsymbol{i}^*_{2dq} j\omega_g L_2. \tag{9}$$

A graphical interpretation of (8) and (9) is shown in Fig. 5.

To determine the derivative of the converter current vector $\boldsymbol{d}_{2i}$, representing the direction and rate of change of the current vector $\boldsymbol{i}_{2dq}$, the (8) must be transformed

$$\boldsymbol{d}_{2i} = \frac{d}{dt}\boldsymbol{i}_{2dq} = \boldsymbol{d}_{2u}/L_2. \tag{10}$$

The discrete operation of ac–dc converters relies on the ability to change voltage vectors at the ac terminals at regular, predefined intervals. This is associated with the cyclic nature of the converter's digital control system. It is when signal acquisition is renewed, and the next iteration of the control algorithm is executed. Hence, the sampling time is defined as

$$T_s = \frac{1}{f_s} \tag{11}$$

where f_s is the measurement system's sampling frequency.

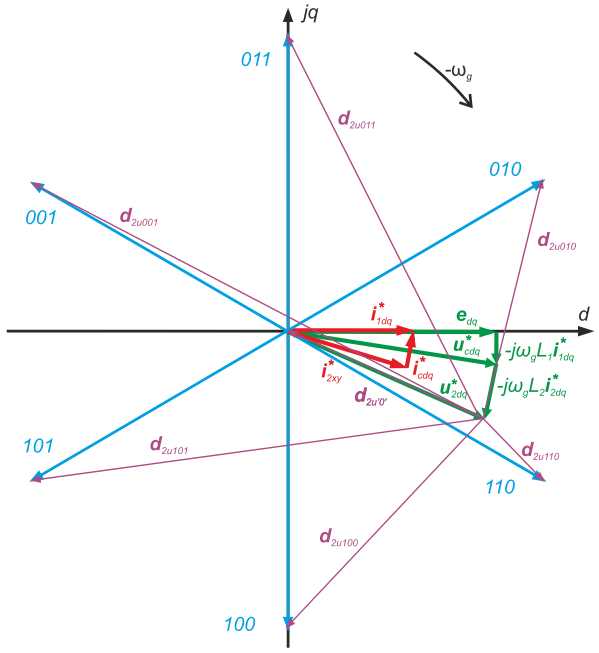

Fig. 5. Graphical interpretation of $\boldsymbol{d}_{2u}$ vectors proportional to the derivative of the current $\boldsymbol{i}_{2dq}$ in the reference frame dq rotating with grid pulsation ω_g.

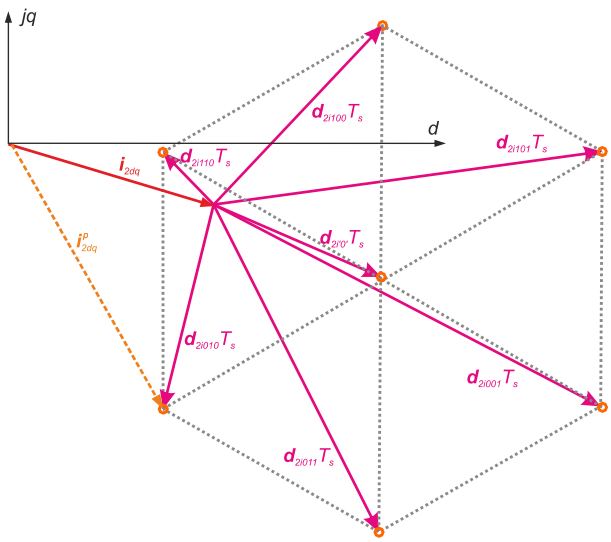

Fig. 6. Potential places to move the $\boldsymbol{i}_{2dq}$ vector during single T_s by selecting a single converter voltage vector.

During a single sampling period, using only one available voltage vector of the converter, it is possible to determine the predicted position of the head of the converter current vector $\boldsymbol{i}^p_{dq}$ at the end of the considered sampling period. To achieve this, the equation below should be used

$$\boldsymbol{i}^p_{2dq} = \boldsymbol{i}_{2dq} + \boldsymbol{d}_{2i} T_s. \tag{12}$$

Graphical interpretation of (12) for an example converter voltage vector is shown in Fig. 6. After one sampling time, the head of the $\boldsymbol{i}_{2dq}$ can reach positions marked by orange circles.

With knowledge of possible new positions of the $\boldsymbol{i}_{2dq}$, its impact on the $\boldsymbol{u}_{cdq}$ can be determined. To achieve this, the transformed (7) should be used

$$\boldsymbol{d}_{uc} = \frac{d}{dt}\boldsymbol{u}_c = \frac{\boldsymbol{i}_{1dq} - \boldsymbol{i}^p_{2dq} - j\omega_g C\boldsymbol{u}_{cdq}}{C}. \tag{13}$$

To determine voltage change on the capacitor C based on the given equation, the following assumptions must be made.

1) The change in current $\boldsymbol{i}_{1dq}$ for a single sampling period T_s is close to zero

$$\boldsymbol{d}_{1i} \approx 0. \tag{14}$$

2) Changes in the current vector $\boldsymbol{i}_{2dq}$ are significantly faster than the rate of changes in the vector $\boldsymbol{i}_{1dq}$

$$\boldsymbol{d}_{2i} >> \boldsymbol{d}_{1i}. \tag{15}$$

Considering the above, displacing the $\boldsymbol{i}_{2dq}$ vector described by (12) results in a voltage change on capacitor C

$$\boldsymbol{d}_{uc} = \frac{\boldsymbol{i}_{1dq} - \boldsymbol{i}_{2dq} - j\omega_g C\boldsymbol{u}_{cdq} - \left(\boldsymbol{i}_{1dq} - \boldsymbol{i}^p_{2dq} - j\omega_g C\boldsymbol{u}_{cdq}\right)}{C}$$
$$= \frac{\boldsymbol{i}^p_{2dq} - \boldsymbol{i}_{2dq}}{C}. \tag{16}$$

After one sampling period, T_s, it can obtain a new position in the dq plane, described by the relation

$$\boldsymbol{u}^p_{cdq} = \boldsymbol{u}_{cdq} + \boldsymbol{d}_{uc}T_s. \tag{17}$$

Emphasizing the assumptions about the rate of changes in currents $\boldsymbol{i}_{1dq}$ and $\boldsymbol{i}_{2dq}$ described by (14) and (15), it is considered that the change in the $\boldsymbol{i}_{1dq}$ for one sampling period T_s has a negligible impact on the voltage on filter capacitor C. The change of the $\boldsymbol{u}_{2dq}$ causes a change in the $\boldsymbol{i}_{2dq}$ vector's position, which, in turn, causes a change in the $\boldsymbol{u}_{cdq}$ vector's position.

Using an analogy to analyze the impact of the $\boldsymbol{u}_{2dq}$ on the $\boldsymbol{i}_{2dq}$, an analysis was conducted on the influence of changes in the $\boldsymbol{u}_{cdq}$ on the $\boldsymbol{i}_{1dq}$. It was assumed that the primary influence on changes in the $\boldsymbol{i}_{1dq}$ has $\boldsymbol{u}_{cdq}$. This assumption arises from the higher dynamics of changes in the $\boldsymbol{u}_{cdq}$ (17) compared to changes in the $\boldsymbol{e}_{dq}$.

In the steady state of the *LCL* filter, the current derivative component related to the inductance L_1 in (5) is equal to 0. Thus, based on the mentioned expression, we can write

$$\boldsymbol{u}_{cdq} = \boldsymbol{e}_{dq} - j\omega_g L_1 \boldsymbol{i}_{1dq}. \tag{18}$$

The changes in the position of the $\boldsymbol{u}_{2dq}$ introduced by the converter cause variations in the $\boldsymbol{u}_{cdq}$ voltage, reaching different positions of $\boldsymbol{u}^p_{cdq}$. This is described from (8) to (17). Referring back to (5), we can write

$$L_1\frac{d}{dt}\boldsymbol{i}_{1dq} = \boldsymbol{e}_{dq} - j\omega_g L_1 \boldsymbol{i}_{1dq} - \boldsymbol{u}^p_{cdq}. \tag{19}$$

Next, by substituting (17) with (19) and comparing it with (18), we obtain

$$\boldsymbol{d}_{1u} = L_1\frac{d}{dt}\boldsymbol{i}_{1dq} = -\boldsymbol{d}_{uc}T_s \tag{20}$$

$$\boldsymbol{d}_{1i} = \frac{d}{dt}\boldsymbol{i}_{1dq} = \boldsymbol{d}_{1u}\frac{1}{L_1} \tag{21}$$

$$\boldsymbol{i}^p_{1dq} = \boldsymbol{i}_{1dq} + \boldsymbol{d}_{1i}T_s \tag{22}$$

where

$\boldsymbol{d}_{1u}$ – quantity proportional to the derivative of the $\boldsymbol{i}_{1dq}$,
$\boldsymbol{d}_{1i}$ – a derivative of the $\boldsymbol{i}_{1dq}$ describing the direction and rate of changes in the $\boldsymbol{i}_{1dq}$,
$\boldsymbol{i}^p_{1dq}$ – predicted position of the grid current vector resulting from the change in voltage on filtering capacitors due to activate one of the available voltage vectors of the converter for a single sampling period.

Utilizing (12) to (22) allows for predicting voltages and currents in the *LCL* filter as the system's response to activating one of the available converter vectors for a single sampling period. This control approach is typical for methods within the FCS-MPC group. Control algorithms from this group have two significant drawbacks. The first is the inability to direct the grid current vector to the desired vector position within one control period. The second drawback pertains to variable switching frequencies, causing difficulty in selecting parameters for the filter connecting the converter to the power grid. In such a scenario, the challenge lies in choosing passive filter element parameters that achieve maximum damping without amplifying current distortions due to the matching of switching frequencies to the resonant frequencies of the filter.

IV. Description of the Proposed Control Method

This chapter introduces an author-developed CCS C-BMPC for a two-level, three-phase ac–dc converter coupled to the grid through an *LCL* filter. The proposed control method aims to eliminate the drawbacks of FCS-MPC methods. Analyzing (8) to (22) in reverse order makes it possible to determine a change of $\boldsymbol{i}_{2dq}$ that theoretically compensates the $\boldsymbol{i}_{1dq}$ error to zero during a single control period. It is assumed that the predicted position of the grid current vector $\boldsymbol{i}^p_{1dq}$ at the end of the control period T_s should be identical to the position of the set grid current vector $\boldsymbol{i}^s_{1dq}$, i.e.,

$$\boldsymbol{i}^p_{1dq} = \boldsymbol{i}^s_{1dq}. \tag{23}$$

Based on (22) and substituting (23) into it, the relationship determining the grid current error $\Delta\boldsymbol{i}_{1dq}$ is obtained

$$\Delta\boldsymbol{i}_{1dq} = \boldsymbol{i}^s_{1dq} - \boldsymbol{i}_{1dq}. \tag{24}$$

Assuming that the set voltage vector on the filter capacitor $\boldsymbol{u}^s_{cdq}$ is identical to the predicted position of this vector denoted as $\boldsymbol{u}^p_{cdq}$ in (17), and considering (20) in that equation, the following differential equation is obtained:

$$\Delta\boldsymbol{u}^s_{cdq} = \boldsymbol{u}^s_{cdq} - \boldsymbol{u}_{cdq} = -\frac{\Delta\boldsymbol{i}_{1dq}}{T_s}L_1. \tag{25}$$

The transformed (13) into differential form allows determining the set position of the converter current vector $\boldsymbol{i}^s_{2dq}$ (the reference vector $\boldsymbol{i}^s_{2dq}$ is identical to the predicted vector $\boldsymbol{i}^p_{2dq}$) that theoretically compensates the control error to zero during a

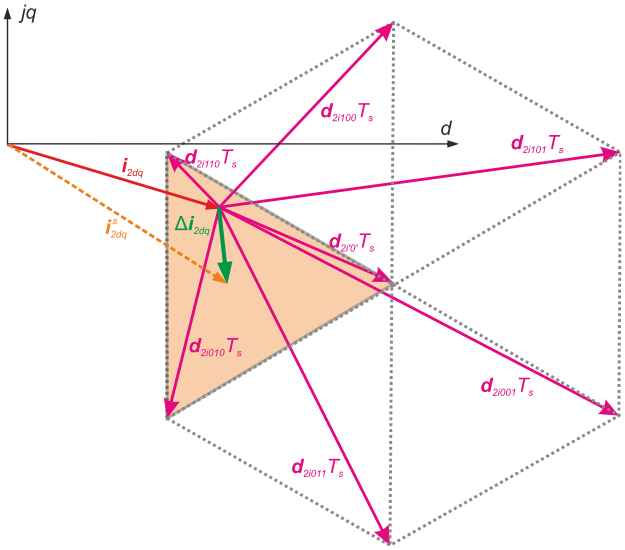

Fig. 7. Ability to move the converter current vector $\boldsymbol{i}_{2dq}$ with three converter voltage vectors during single T_s.

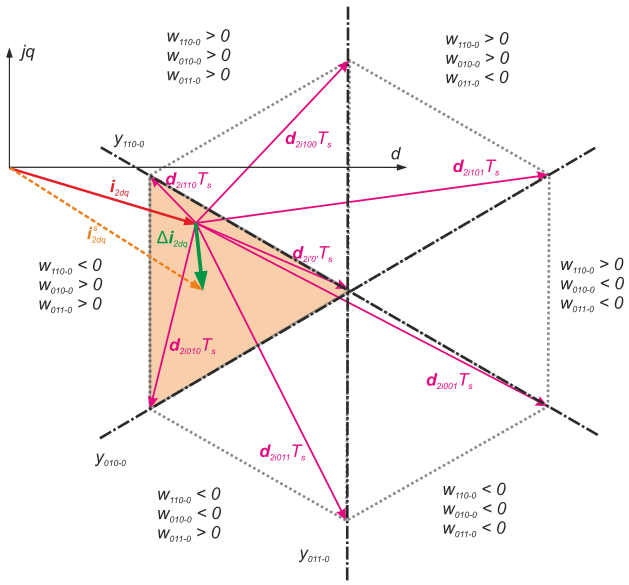

Fig. 8. Principle of determining converter voltage vectors used in modulation.

single T_s period

$$\boldsymbol{i}^s_{2dq} = \boldsymbol{i}_{1dq} - j\omega_g C\boldsymbol{u}_{cdq} - \frac{\Delta\boldsymbol{u}^s_{cdq}}{T_s}C. \tag{26}$$

Utilizing the difference between the specified position of the converter current vector $\boldsymbol{i}^s_{2dq}$ and its current position $\boldsymbol{i}_{2dq}$, the error of the converter current vector $\Delta\boldsymbol{i}_{2dq}$ is defined

$$\Delta\boldsymbol{i}_{2dq} = \boldsymbol{i}^s_{2dq} - \boldsymbol{i}_{2dq}. \tag{27}$$

Substituting (26) into (27) and transformations aimed at determining the necessary change in the converter current vector $\Delta\boldsymbol{i}_{2dq}$ to compensate for the voltage error on the filtering capacitor $\boldsymbol{u}_{cdq}$, thus achieving zero grid current error $\Delta\boldsymbol{i}_{1dq}$ at the end of a single control period, we obtain the following relation:

$$\Delta\boldsymbol{i}_{2dq} = \boldsymbol{i}_{1dq} - \boldsymbol{i}_{2dq} - j\omega_g C\boldsymbol{u}_{cdq} - \frac{\Delta\boldsymbol{u}^s_{cdq}}{T_s}C. \tag{28}$$

The possibilities of influencing the $\boldsymbol{i}_{2dq}$ using a single converter voltage vector in a single control period are described by relations (8), (10), (11), and (12). By applying a specific voltage vector at the converter output for time T_s, we can predict its final position at the end of the sampling period, as shown in Fig. 6. According to Fig. 6, the head of the converter current vector $\boldsymbol{i}_{2dq}$, after single T_s, can reach positions marked by orange circles. Notice that none of the available voltage vectors results in zeroing the $\Delta\boldsymbol{i}_{2dq}$, i.e., it is unable to move the $\boldsymbol{i}_{2dq}$ to its desired value $\boldsymbol{i}^s_{2dq}$. To achieve the set position of the converter current $\boldsymbol{i}^s_{2dq}$ within a single T_s, a minimum of three vectors must be used during this time. Employing three-vector modulation increases the possibilities of shaping the reproduced $\boldsymbol{i}_{2dq}$.

In Fig. 7, the area of the equilateral triangle (sector) formed by the two active vectors 010 and 110, and the zero vector '0' is shaded with an orange background. This highlighted region, resulting from the modulation of the specified three vectors, is the space where the head of the $\boldsymbol{i}_{2dq}$ current vector can be placed arbitrarily at the end of a single T_s. The selection of vectors allowing the elimination of the controlled $\boldsymbol{i}_{2dq}$ error depends on the current positions of the vectors $\boldsymbol{u}_{2dq}$, $\boldsymbol{u}^*_{2dq}$, and the $\Delta\boldsymbol{i}_{2dq}$.

Determining, which derivative vectors will be used and for how long to move the $\boldsymbol{i}_{2dq}$ to the $\boldsymbol{i}^s_{2dq}$ position requires a series of geometrically described actions. First, it is necessary to determine the position of the head of the $\boldsymbol{i}^s_{2dq}$ on the hexagon plane and thus specify, which derivative vectors will be used. To achieve this, the positions of the heads of three consecutive current derivative vectors from active converter vectors, such as $\boldsymbol{d}_{2i110}$, $\boldsymbol{d}_{2i010}$, and $\boldsymbol{d}_{2i011}$, as well as the current derivative of the $\boldsymbol{d}_{2i'0'}$ from the zero vector of the converter, are used. This is done by determining three lines labeled $y_{110\text{-}0}$, $y_{010\text{-}0}$, and $y_{011\text{-}0}$ through these four points. The situation is illustrated in Fig. 8.

These lines divide the complex plane into sectors. The belonging of the head of the $\boldsymbol{i}^s_{2dq}$ to a sector is determined by establishing equations for the lines $_{y110\text{-}0}$, $_{y010\text{-}0}$, and $_{y011\text{-}0}$. The calculation of the coefficients $A_{xxx\text{-}x}$, $B_{xxx\text{-}x}$, and $C_{xxx\text{-}x}$ of the line equation in general form $A_{x\text{-}xxx}x + B_{x\text{-}xxx}y + C_{x\text{-}xxx} = 0$ is performed using (29) and the knowledge of the coordinates of two points through which the sought line passes

$$\begin{aligned} A_{xxx-x} &= y_{xxx} - y_x \\ B_{xxx-x} &= x_x - x_{xxx} \\ C_{xxx-x} &= (x_x - x_{xxx}) \cdot y_{xxx} + (y_{xxx} - y_x) \cdot x_{xxx}. \end{aligned} \tag{29}$$

For the determined equations of lines $y_{110\text{-}0}$, $y_{010\text{-}0}$, and $y_{011\text{-}0}$ in general form, the coordinates of the head point of the current error vector $\Delta\boldsymbol{i}_{2dq}$ are substituted

$$w_{xxx-x} = A_{xxx-x}x + B_{xxx-x}y + C_{xxx-x}. \tag{30}$$

This yields results $w_{110\text{-}0}$, $w_{010\text{-}0}$, and $w_{011\text{-}0}$, whose signs unequivocally determine the position of the examined point

TABLE I
ASSIGNING VECTORS IN THREE-VECTOR MODULATION

Sector	$w_{110\text{-}0}$	$w_{010\text{-}0}$	$w_{011\text{-}0}$	Set of vectors for three-vector modulation
1	<0	>0	>0	u_{110}, u_{010}, $u_{0'}$
2	<0	<0	>0	u_{010}, u_{011}, $u_{0'}$
3	<0	<0	<0	u_{011}, u_{001}, $u_{0'}$
4	>0	<0	<0	u_{001}, u_{101}, $u_{0'}$
5	>0	>0	<0	u_{101}, u_{100}, $u_{0'}$
6	>0	>0	>0	u_{100}, u_{110}, $u_{0'}$

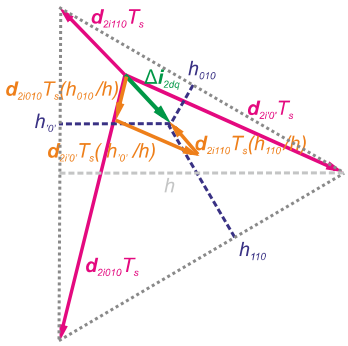

Fig. 9. Determining the activation times for individual voltage vectors of the converter during one sampling period T_s.

relative to the specified lines. With this information, two adjacent vectors to the head position of the $\Delta \boldsymbol{i}_{2dq}$, representing the derivatives of the current $\boldsymbol{d}_{2ixxx}$ from the active voltage vectors of the converter, and one vector representing the current derivative $\boldsymbol{d}_{2i'0'}$ from the zero voltage vector of the converter, are determined. Information on the modulation voltage vectors used by the converter depending on the sector containing the head of the $\Delta \boldsymbol{i}_{2dq}$ is provided in Table I.

To move the $\Delta \boldsymbol{i}_{2dq}$ to zero (see Fig. 9) within single T_s, one should follow the principles outlined in the rest of the chapter. Applying these principles results in displacing the head of the controlled variable vector, in this case, the head of the $\boldsymbol{i}_{2dq}$, to the setpoint position $\boldsymbol{i}^s_{2dq}$ (see Fig. 8), which corresponds to the head of the error vector $\Delta \boldsymbol{i}_{2dq}$ in Fig. 9. The trajectory of the $\boldsymbol{i}_{2dq}$ vector head position changes is highlighted in orange on the discussed figure.

Equation (31) can be derived based on geometric relationships. It describes the method for determining the times of using successive derivatives

$$\frac{h_{010}}{h} \cdot T_s + \frac{h_{0'}}{h} \cdot T_s + \frac{h_{110}}{h} \cdot T_s = T_s. \tag{31}$$

The above is sufficient to calculate three absolute values of times t_{110}, t_{010}, and $t_{0'}$ according to the equation below. These times determine the times of using individual voltage vectors within one control period T_s

$$T_s = t_{0'} + t_{110} + t_{010}$$

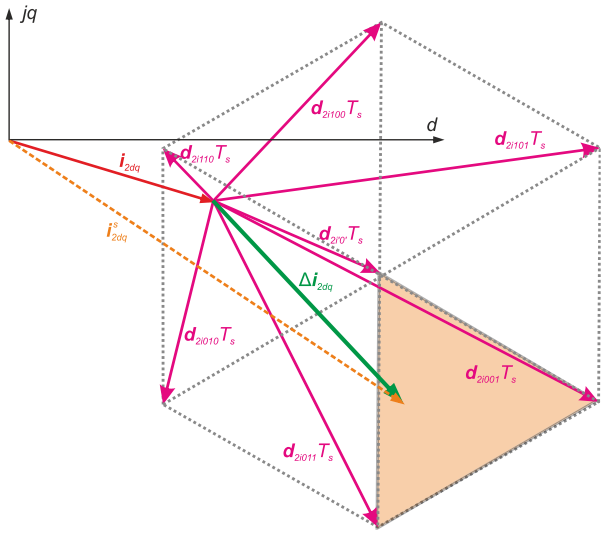

Fig. 10. Options to minimize the converter current error vector $\Delta \boldsymbol{i}_{2dq}$ with three voltage vectors during one sampling period T_s.

$$\text{where}: \quad t_{0'} = \frac{h_{0'}}{h} \cdot T_s, t_{110} = \frac{h_{110}}{h} \cdot T_s, t_{010} = \frac{h_{010}}{h} \cdot T_s. \tag{32}$$

The t_{110}, t_{010}, and $t_{0'}$, determined in this way, sum up the value T_s. In the definition of $\boldsymbol{d}_{2i}$ described by (10), the dependence of this vector on the derivative vector of the converter voltage vector $\boldsymbol{d}_{2u}$ defined in (8) is indicated. Therefore, by applying specific voltage vectors $\boldsymbol{u}_{2dq}$ (on which the considered sector of the hexagon is stretched) according to (32), we achieve the zeroing of the $\Delta \boldsymbol{i}_{2dq}$

$$\Delta \boldsymbol{i}_{2dq} = t_{0'} \boldsymbol{d}_{2i'0'} + t_{110} \boldsymbol{d}_{2i110} + t_{010} \boldsymbol{d}_{2i010}. \tag{33}$$

During transient states of the converter, after a step change in the $\boldsymbol{i}^s_{1dq}$, the control error $\Delta \boldsymbol{i}_{2dq}$ can assume values greater than in the previously discussed situation. Representing this graphically (see Fig. 10), the head of the vector may be in a sector different from its tail.

In this scenario, examining the signs of the results of linear (30) with substituted coordinates of the head of the $\Delta \boldsymbol{i}_{2dq}$ reveals that a different set of voltage vectors will be used for modulation (see Table I). However, the principle of calculating the activation times of individual converter voltage vectors will be identical to the case discussed in Fig. 9. The analyzed situation is depicted in Fig. 11.

Another case to consider is a sudden change in the $\boldsymbol{i}^s_{1dq}$. The head of the $\Delta \boldsymbol{i}_{2dq}$ may fall outside the hexagon (see Fig. 12).

In this operating state of the converter, it is impossible to compensate the $\Delta \boldsymbol{i}_{2dq}$ to zero during a single T_s. This is due to the length of the $\Delta \boldsymbol{i}_{2dq}$ being greater than all available current derivative vectors $\boldsymbol{d}_{2i}$. To confirm that the position of the head of the $\Delta \boldsymbol{i}_{2dq}$ is outside the hexagon, the following condition must be satisfied:

$$h < h_{011} + h_{001}. \tag{34}$$

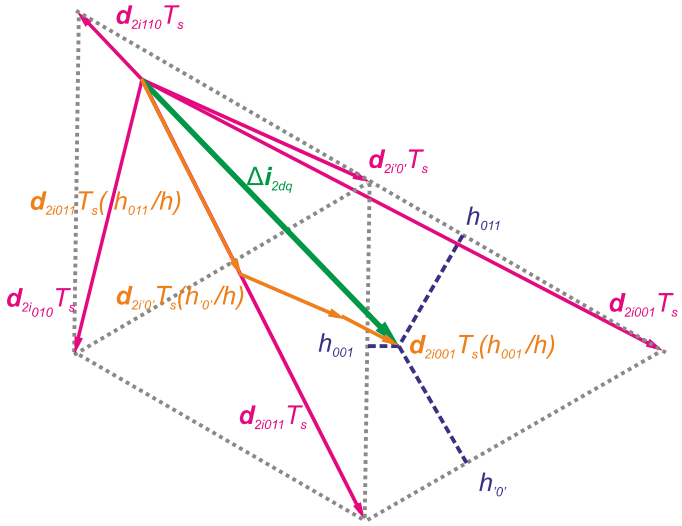

Fig. 11. Example of minimizing the converter current error vector $\Delta \boldsymbol{i}_{2dq}$ with three voltage vectors during one sampling period T_s.

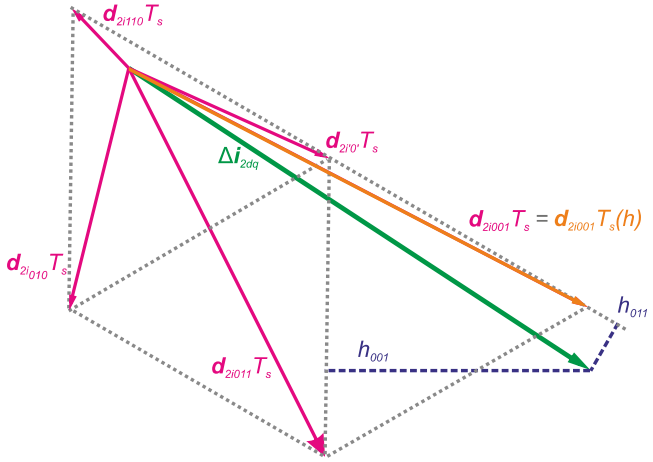

Fig. 12. Options to minimize the converter current error vector $\Delta \boldsymbol{i}_{2dq}$ with one voltage vector during one sampling period T_s.

If (34) is met, a different method of determining the switch-on times for individual vectors from the previously selected vector set is used, following the principle below:

1) if $h_{max} = h_{001}$, then: $t_{001} = T_s$, $t_{001} = 0$, $t_{0'} = 0$,
2) if $h_{max} = h_{011}$, then: $t_{001} = 0$, $t_{001} = T_s$, $t_{0'} = 0$.

Selecting one active vector in this way for a single T_s minimizes the $\Delta \boldsymbol{i}_{2dq}$. The goal is to bring the head of the $\Delta \boldsymbol{i}_{2dq}$ inside the hexagon and then regulate the current using three-vector modulation, following the earlier principles.

The last step of the presented algorithm is to convert the obtained absolute times for using individual voltage vectors into control pulses for the transistors of the individual phase bridges. The modulation method, e.g., SVM or three-phase sinusoidal modulation, can be arbitrary. In this article, a three-phase modulator is chosen for this purpose. With this, the discussion of the proposed control method utilizing the model equations and PWM modulation concludes. Due to the flexibility in moving

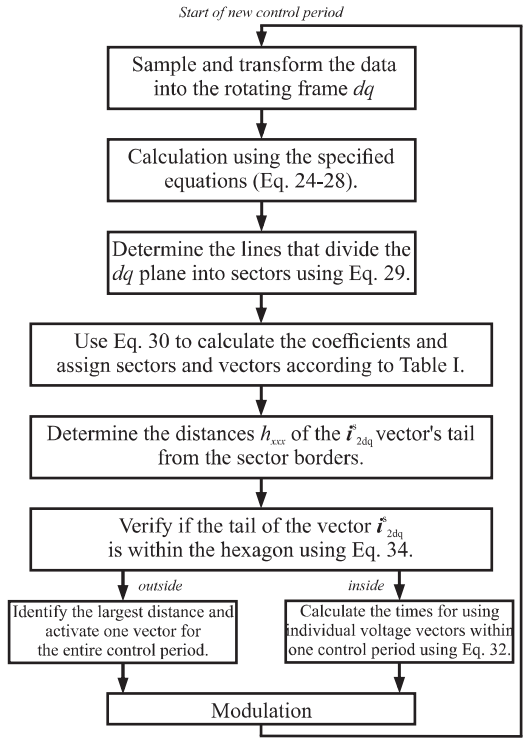

Fig. 13. Graph illustrating the execution of the successive steps of the CCS C-BMPC control method.

the head of the $\boldsymbol{i}_{2dq}$ within the hexagon spanned by the current derivative vectors $\boldsymbol{d}_{2i}$, this method can be classified as a continuous control set method. When the $\Delta \boldsymbol{i}_{2dq}$ lies within the hexagon boundaries, three-vector modulation is applied, theoretically allowing for zero $\Delta \boldsymbol{i}_{2dq}$ at the end of a single T_s. In transient states, the converter controlled by this method exhibits a fast response, utilizing single vectors throughout the control period, which quickly approaches the $\Delta \boldsymbol{i}_{2dq}$ to the value of 0.

Fig. 13 presents a summary graph illustrating the execution of the proposed algorithm's successive steps.

V. Simulation Studies of the Proposed Control Method

The simulation model for the voltage converter coupled to the grid was developed using the MATLAB/Simulink environment. The model structure replicates the block diagram shown in Fig. 4. The key parameters of the simulated system are listed in the Table II.

Validating the *LCL* filter design involves calculating its resonance frequencies: the main resonance frequency f_r, resonance frequency f_{r1} associated with elements L_1 and C, and resonance frequency f_{r2} associated with elements L_2 and C. These values should fall within the range

$$10 \cdot f_n < f_r < 0.5 \cdot f_m. \tag{35}$$

The following dependencies determine the resonant frequencies of the used *LCL* filter:

$$f_r = \frac{1}{2\pi}\sqrt{\frac{L_1 + L_2}{L_1 L_2 C}}$$

TABLE II
KEY PARAMETERS OF THE SIMULATION SYSTEM

Parameter	Value
Power grid parameters $U_{L\text{-}N}$, f_n	230 V, 50 Hz
DC-link voltage U_{dc}	640 V
The inductance of the filter inductor L_1	1,83 mH
The inductance of the filter inductor L_2	3,4 mH
The capacitance of the filter capacitors C	10 µF
Control system sampling time T_s	200 µs
Modulation frequency f_m	5 kHz

$$= \frac{1}{2\pi}\sqrt{\frac{1.83\cdot 10^{-3}+3.4\cdot 10^{-3}}{1.83\cdot 10^{-3}\cdot 3.4\cdot 10^{-3}\cdot 10\cdot 10^{-6}}} = 1.46\,[\text{kHz}] \tag{36}$$

$$f_{r1} = \frac{1}{2\pi}\sqrt{\frac{1}{L_1 C}} = \frac{1}{2\pi}\sqrt{\frac{1}{1.83\cdot 10^{-3}\cdot 10\cdot 10^{-6}}} = 1.17\,[\text{kHz}] \tag{37}$$

$$f_{r2} = \frac{1}{2\pi}\sqrt{\frac{1}{L_2 C}} = \frac{1}{2\pi}\sqrt{\frac{1}{3.4\cdot 10^{-3}\cdot 10\cdot 10^{-6}}} = 863\,[\text{Hz}]. \tag{38}$$

Calculated values of resonance frequencies satisfy the condition presented in (35), completing the design of the grid filter coupling the converter to the grid.

The study was conducted with a specified value $i_{1d}^s = 15$ A ($P = 7.5$ kW) and $i_{1q}^s = 0$ A ($Q = 0$ var). To observe the regulation process using the presented method, waveforms of components d and q of the $\boldsymbol{i}_{1dq}$, $\boldsymbol{i}_{1dq}^s$, $\boldsymbol{u}_{cdq}$, $\boldsymbol{i}_{2dq}$, and $\boldsymbol{e}_{dq}$ are included. Fig. 14 depicts the components recorded in the rotating reference frame dq synchronized to the $\boldsymbol{e}_{dq}$, aligned with the d-axis. This illustration showcases the operation of the developed control algorithm with symmetrical, undistorted voltage supplied from the grid.

Analysis of the i_{1d} waveform, recorded and shown in Fig. 14, revealed minor fluctuations. The maximum value of the i_{1d} is 15.22 A, while the minimum is 14.92 A. In the recorded time window, the i_{1q} has a maximum value of 0.17 A and a minimum value of -0.16 A.

The waveforms of the i_1 are symmetrical (see Fig. 15). These current waveforms do not exhibit phase shift relative to the corresponding waveforms of the grid voltages. Furthermore, comparing the waveforms of i_1 and i_2 on the indicated plot reveals high effectiveness in attenuating current ripples, a characteristic feature of an *LCL* filter.

Harmonic analysis of the phase current i_{1u} is presented in Fig. 16. The results indicate that practically no higher harmonics associated with the resonant frequencies of the *LCL* filter, as described by (36), (37), and (38), are present in the power grid current. Their amplitude does not exceed 0.1% of the fundamental harmonic amplitude. Attention should be paid to the characteristic peaks in the spectrum of the analyzed current related to the operating frequency of the used three-phase PWM

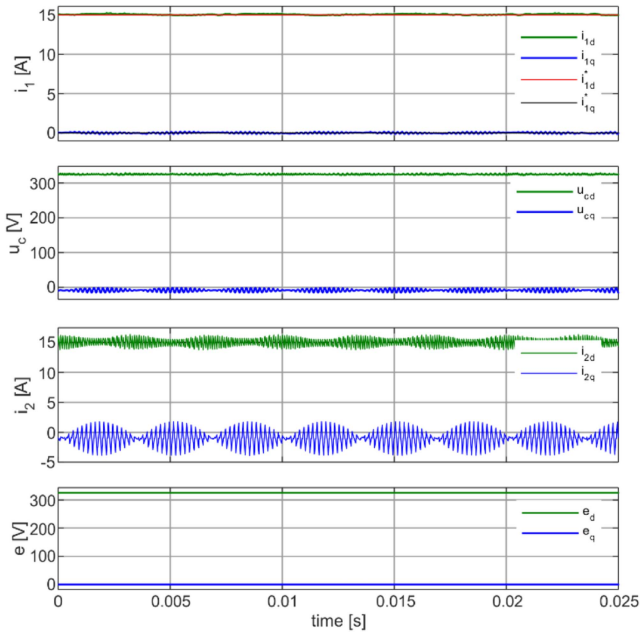

Fig. 14. Waveforms of vectors components in the simulated converter system with the $i_{1d}^s = 15$ A.

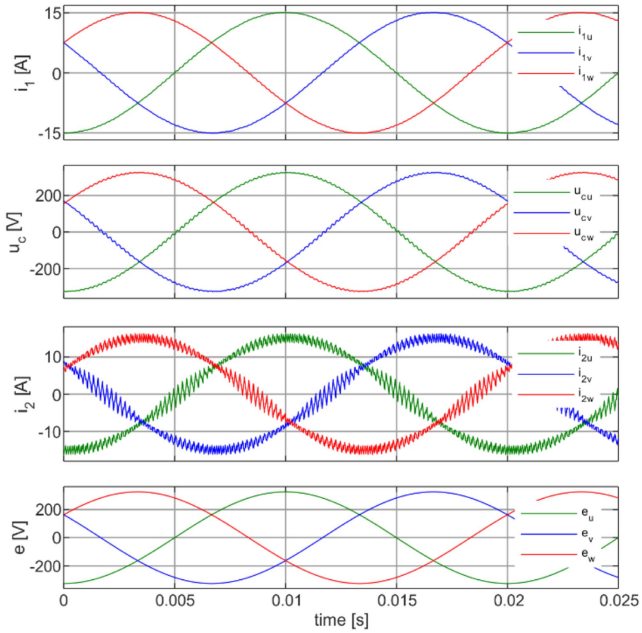

Fig. 15. Waveforms of phase quantities in the simulated converter system with the $i_{1d}^s = 15$ A.

modulator. These peaks are concentrated around the multiples of the modulation frequency (5 kHz). Spectrum components related to the modulator operation are prominent in Fig. 15 in the currents i_2. This is confirmed by comparing the corresponding harmonics presented in the spectrum of i_{1u} in Fig. 16 and the spectrum of i_{2u} presented in Fig. 17. The i_{2u} contains components associated with the modulator at approximately 4% of the fundamental harmonic amplitude. The same components

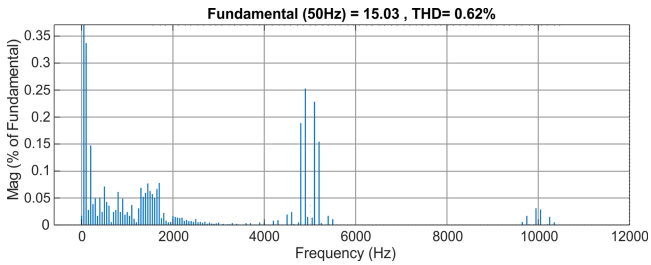

Fig. 16. Spectrum of the $i_{1\,u}$ in the simulated system with the $i^s_{1d} = 15$ A.

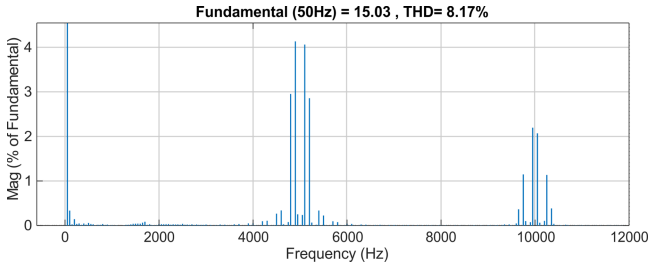

Fig. 17. Spectrum of the $i_{2\,u}$ in the simulated system with the $i^s_{1d} = 15$ A.

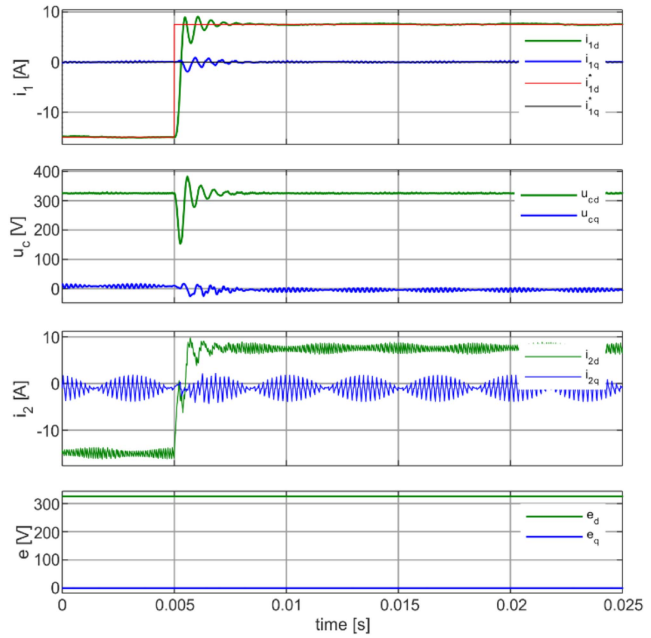

Fig. 18. Waveforms of the vectors components in the simulated converter system, with a step change in the i^s_{1d} from -15 A to 7.5 A.

in the $i_{1\,u}$ do not exceed 0.25% of the fundamental harmonic amplitude.

The next step of control quality verification involved assessing transient states. Studies were conducted, and current and voltage waveforms in the system were recorded, with a step change in the set grid current component i^s_{1d} from -15 A to 7.5 A. Figs. 18 and 19 depict the system's response to the step change in i^s_{1d} from -15 A to 7.5 A.

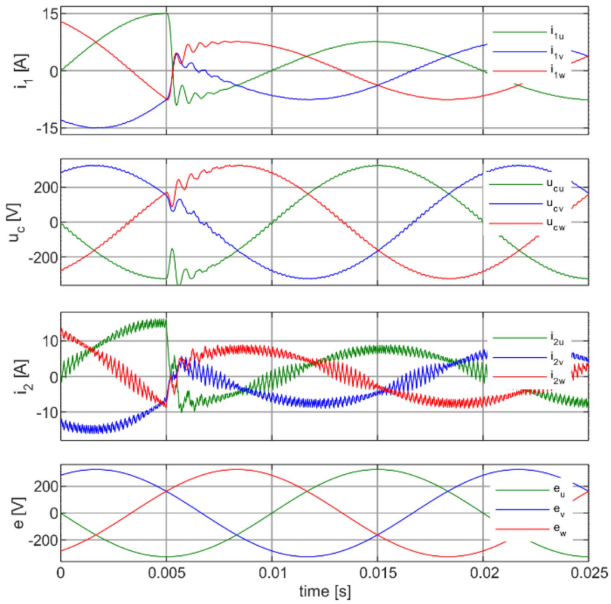

Fig. 19. Waveforms of phase quantities in the simulated converter system, with a step change in the i^s_{1d} -15 A to 7.5 A.

The recorded waveform of the i_{1d} component in Fig. 18 has a rise time t_r of 225 μs. The maximum value of the i_{1d} component in the recorded window is 9.08 A. During the forced step change in the set signal i^s_{1d}, a change in the $i_{1\,q}$ is also observed, reaching a minimum value of -1.91 A during the transient state. The change in the $i_{1\,q}$ in the transient state results from limited influence on the trajectory of the $\boldsymbol{i}_{2dq}$ vector movement. According to Fig. 7 and (12), none of the available converter vectors causes the $\boldsymbol{i}_{2dq}$ current vector to move along the error vector $\Delta\boldsymbol{i}_{2dq}$. According to the regulation principle, three vectors are used during single T_s, as shown in Fig. 9. Each of the three selected vectors simultaneously changes the controlled current's d and q components. Additionally, attention should be paid to the waveforms of the u_{cd} and u_{cq}. In this case, the u_{cd} component decreases to a minimum value of 153.3 V during the transient.

Next, the algorithm's response to asymmetric power supply conditions was tested (see Fig. 20). The voltage source replicated three sinusoidal waveforms. For time $<$ 20 ms, the U phase voltage was reduced to 90%; for time $>$ 20 ms, it was decreased to 20% of the nominal amplitude value. While the supply voltage asymmetry remains within normative conditions (time $<$ 20 ms in Fig. 20), amplitude asymmetry in grid currents is imperceptible. However, a distinct asymmetry in current amplitudes is observed during a deep voltage sag (time t $>$ 20 ms in Fig. 19). Considering this it is acknowledged that the algorithm adequately maintains control over currents and voltages in the studied system, ensuring the converter's safe operation during significant supply voltage asymmetry.

Besides voltage asymmetry, a common occurrence in the grid is the distortion of phase voltages due to nonlinear loads. The fifth and seventh harmonics, each with amplitudes equal to 5%

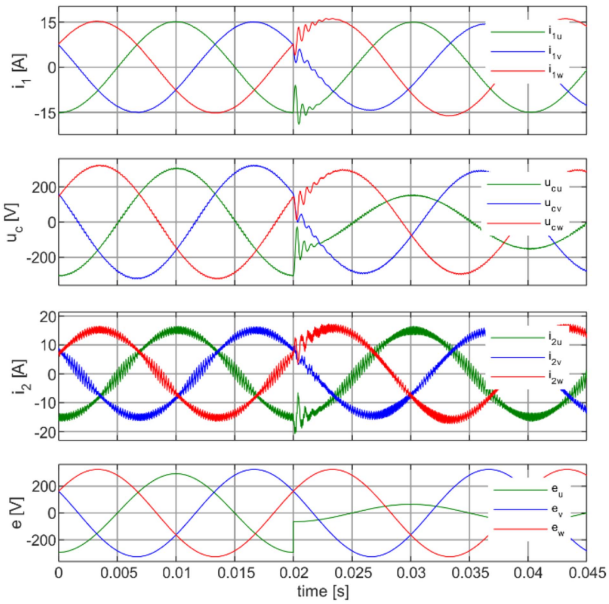

Fig. 20. Waveforms of phase quantities in the simulated converter system, with asymmetric supply ($E_U = 0{,}9U_{L\text{-}N}$, $E_V = E_W = U_{L\text{-}N}$ for time ≤ 20 ms and $E_U = 0{,}2U_{L\text{-}N}$, $E_V = E_W = U_{L\text{-}N}$ for time > 20 ms).

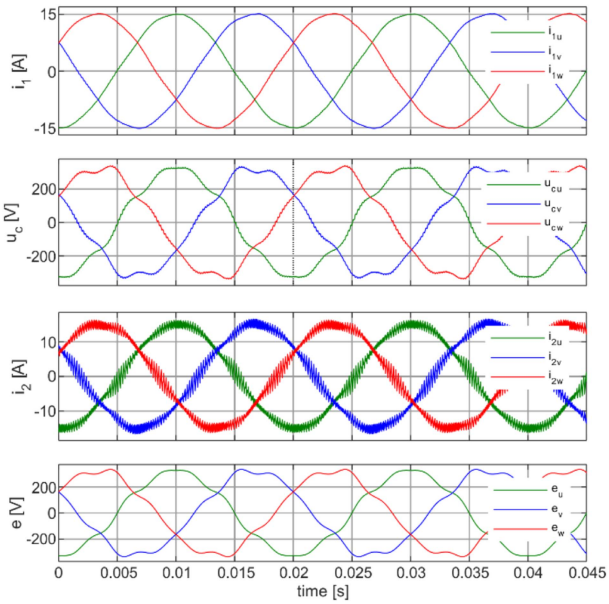

Fig. 21. Waveforms of phase quantities in the simulated converter system, with distorted grid voltage by adding 5% of the fifth and seventh harmonics.

of the fundamental harmonic amplitude, were introduced into the sinusoidal supply voltage (see Fig. 21).

As seen in Fig. 21, the generated grid currents are also distorted due to the appearance of higher harmonics in the supply voltage e. The THD for the recorded $i_{1\,u}$ is 1.44%.

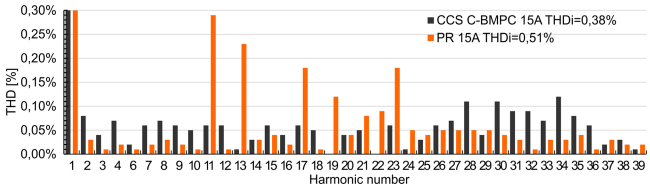

Fig. 22. Spectra of the $i_{1\,u}$ in the simulated systems with CCS C-BMPC and PR controllers and the $i_{1d}^s = 15$ A.

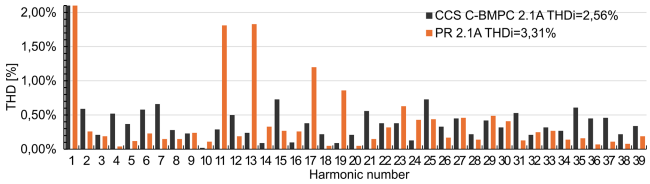

Fig. 23. Spectra of the $i_{1\,u}$ in the simulated systems with CCS C-BMPC and PR controllers, and the $i_{1d}^s = 2.1$ A.

VI. Comparison of the Proposed Method With Typical PR Controller

The proposed control method was compared to the PR controller using simulations in steady-state and transient conditions, as illustrated in the following chapter. When comparing different control methods (e.g., grid current THD), authors usually evaluate them under nominal load conditions. However, all control shortcomings become apparent at low load currents, where the large value of the fundamental harmonic does not mask them. At low currents, errors related to the method of dead time compensation, compensation for delays resulting from the difference between the sampling times of currents and voltages and the moment of control change, and the timing of when the measured quantities are sampled, emerge. In this article, the authors presented a waveform at a low current value (14% of I_n) and compared the result with the PR method.

The structure of the applied PR controller corresponds to the structure presented in [31]. Due to the similarity in tuning principles between linear PI and PR controllers, the settings of the PR controller were selected using the symmetrical optimum method based on the relationships described in [32]. The effectiveness and correctness of using the indicated tuning method in systems with resonant components have been confirmed, among others, in [33]. The converter with PR controller, using the same model and control system parameters, was found to be unstable in the simulation study. In [34], a detailed analysis of the operation of resonant controllers was conducted. The frequency of the controller and modulator should be increased to improve the system's stability. After increasing the operating frequency of the controller and modulator to 20 kHz, system stability was achieved, allowing for a basic comparison of our proposed method with the PR controller.

The first step compared regulation quality in the steady state under a sinusoidal voltage supply. Figs. 22 and 23, respectively, present the spectra of the shaped current at two different setpoint values of the i_{1d}^s component, 15 A and 2.1 A, using the proposed

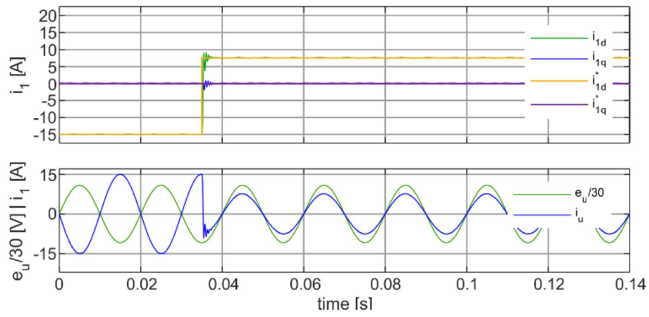

Fig. 24. Selected waveforms in the simulated system with CCS C-BMPC controller during a step change in the i^s_{1d} from −15 A to 7.5 A. Top: set (i^*_{1d} - yellow, i^*_{1d} - magenta) and actual (i_{1d} - green, i_{1q} - blue) grid current vector components values. Bottom: grid current (blue) and voltage (green) in phase *u*.

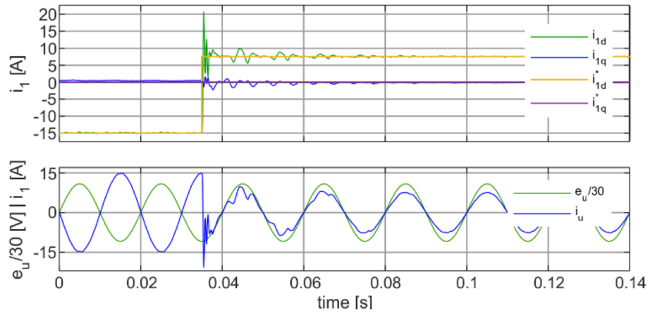

Fig. 25. Selected waveforms in the simulated system with PR controller during a step change in the i^s_{1d} from −15 A to 7.5 A. Top: set (i^*_{1d} - yellow, i^*_{1d} - magenta) and actual (i_{1d} - green, i_{1q} - blue) grid current vector components values. Bottom: grid current (blue) and voltage (green) in phase *u*.

CCS C-BMPC method and the PR method. From Figs. 22 and 23, it can be concluded that the shaped currents have low THD coefficients. In the case of the PR regulator, there is an elevated content of the 9th and 11th harmonics, which are not compensated due to the lack of appropriate regulator modules tuned to these frequencies. It should be noted that in the presented case, the modulation frequency in the model with the PR regulator is four times higher than the modulation frequency in the system with the CCS C-BMPC regulator, resulting in four times smaller current ripples in the filter inductances on the converter side.

The pair of Figs. 24 and 25 present the response of the compared control systems to a change in the setpoint of the grid current vector *d*-component from −15 A to 7.5 A. In the system with the CCS C-BMPC regulator, the grid current overshoot in the presented waveforms after the step change in the setpoint is significantly smaller (see Fig. 24). In the system with the PR regulator (see Fig. 25), the damping time of oscillations is significantly longer, approximately 60 ms.

The resilience of the PR algorithm to asymmetric supply voltage was also investigated. Fig. 26 shows the system's response with the PR regulator to a decrease in the supply voltage in phase *u* to 20% of its nominal value. Under these supply conditions, the PR regulator shapes the current with a THD of 0.96%. The current shaped by the CCS C-BMPC method has a THD parameter of 0.40%. The regulation results in the

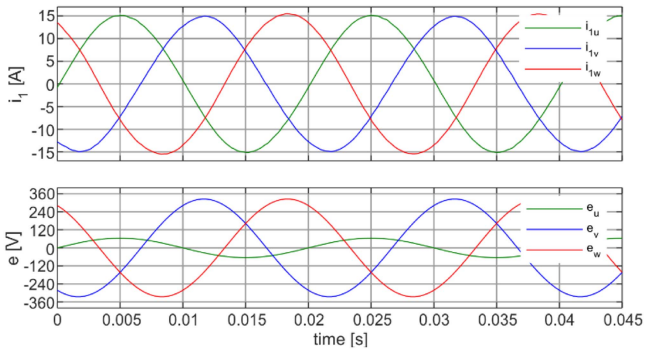

Fig. 26. Phase grid currents (top) and grid voltages (bottom) waveform with PR controller under asymmetric supply ($E_U = 0{,}2U_{L\text{-}N}$, $E_V = E_W = U_{L\text{-}N}$), and $i^s_{1d} = 15$ A.

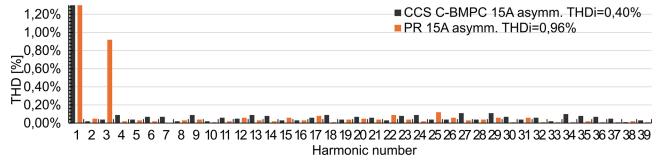

Fig. 27. Comparison of spectra of grid current waveforms with CCS C-BMPC and PR under asymmetric supply ($E_U = 0{,}2U_{L\text{-}N}$, $E_V = E_W = U_{L\text{-}N}$), and $i^s_{1d} = 15$ A.

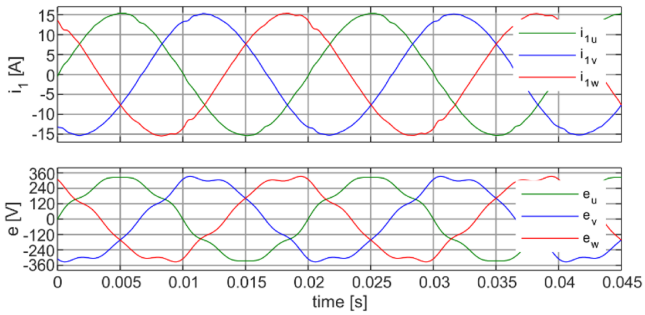

Fig. 28. Phase grid currents (top) and grid voltages (bottom) waveforms with PR controller under distorted grid voltage by adding 5% of the fifth and seventh harmonics, and $i^s_{1d} = 15$ A.

system with the CCS C-BMPC regulator are shown in Fig. 20 in Section V. The current spectra shaped by both methods are presented in Fig. 27. In the PR method, a nearly twofold increase in THD was noted compared to the undisturbed supply condition (see Fig. 22). During significant supply asymmetry, the current shaped by the PR method showed a substantial content of the third harmonic, which does not occur in the system with the CCS C-BMPC regulator.

The PR regulator's response to higher harmonics in the supply voltage is shown in Fig. 28. The fifth and seventh harmonics with amplitudes equal to 5% of the fundamental harmonic amplitude were added to the supply voltage. This caused an increase in the THD of the shaped grid current to 1.16%. The spectrum of the grid current showed an elevated content of odd harmonics not attenuated by the regulator, particularly the 9th and 11th harmonics. Under the same power supply conditions,

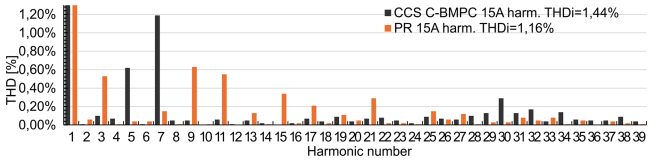

Fig. 29. Comparison of spectra of grid current with CCS C-BMPC and PR under distorted grid voltage by adding 5% of the fifth and seventh harmonic, and $i_{1d}^{s} = 15$ A.

using the CCS C-BMPC regulator, a slightly worse THD of the shaped current was obtained, equal to 1.44% (see Fig. 29). The presence of the fifth and seventh harmonic components was noted, corresponding to the introduced disturbance in the supply voltage. The time waveforms of currents and voltages in the simulated system with the proposed regulator are shown in Fig. 21 in Section V.

It should be noted that the converter with a PR controller and a modulator operating at four times the frequency has worse grid current THD (see Figs. 22 and 23), higher losses, and lower efficiency than the CCS C-BMPC method.

VII. Controller Stability Despite Parameters Incompatibility

Linear controllers have long been a proven solution, extensively described in the literature and applied in practical applications. Their description utilizes small signal models and determines frequency characteristics. However, our approach to designing control systems differs. We employ well-known, verified equations describing the converter model connected to the grid via a selected filter. Subsequently, we geometrically determine the appropriate switching times of individual transistors to theoretically compensate for the converter current's control error to zero within one period. Introducing a nonlinear element into the control loop and utilizing geometric relationships to determine the control voltage for the modulator based on current-scale signals precludes the use of common methods of control system analysis. For this reason, the observation of frequency characteristics has not been presented here.

Fig. 30 contains selected waveforms of the converter current, grid current, and voltage on the filtering capacitor in a system with the CCS C-BMPC regulator during a step change of i_{1d}^{s} from −15 A to 7.5 A for eight different cases of model parameter detuning from nominal parameters. The supply voltage was sinusoidal in all cases.

Studies have confirmed the stability of the control system using the CCS C-BMPC regulator. It was observed that reducing the values of the filtering capacitance and inductance on the converter side negatively affects the quality of regulation. On the other hand, increasing these parameters contributes to a faster achievement of the steady state after a change in the current setpoint.

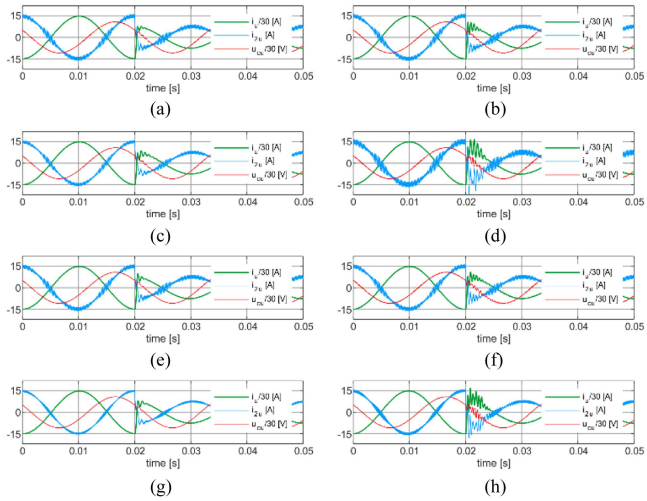

Fig. 30. Waveforms of phase *u* grid current (green), inverted phase *u* converter current, phase *v* capacitor voltage a step change in the i_{1d}^{s} from −15 A to 7.5 A, with modified *LCL* filter parameters: (a) L_1' = 130% L_1; (b) L_1' = 70%L_1; (c) L_2' = 130%L_2; (d) L_2' = 70%L_2; (e) C' = 130%C; (f) C' = 70%C; (g) L_1' = 120%L_1, L_2' = 120%L_2 and C' = 120%C; (h) L_1' = 80%L_1, L_2' = 80%L_2 and C' = 80%C.

TABLE III
Key Parameters of the Experimental System

Part	Model
DC-link circuit	EPCOS B43508-A9108-M (2 mF in total)
The filter inductor L_1	CNW903/16 (1.83 mH)
The filter inductor L_2	CNW933/16 (3.4 mH)
The filter capacitors C	10 μF
Control system	DSP ADSP-21369 + FPGA Xilinx Spartan3
Power grid simulator	California Instruments MX30-3Pi

VIII. Experimental Studies of the Proposed Control Method

Laboratory tests of the proposed control method were conducted on a setup comprising the parameters presented in Tables II and III.

Results in this study were recorded using a Tektronix DPO7054C oscilloscope and Yokogawa WT-1800 power analyzer. THD measurements are values determined by the power analyzer. The laboratory setup is shown in Fig. 31.

Laboratory tests were conducted in two stages. The first aimed to document and verify grid current parameters in static states under various supply conditions:

1) with symmetrical supply voltage (see Figs. 32, 33, and 34),
2) and with asymmetric supply, reducing the amplitude of phase *U* by 50% compared to the other phases (see Fig. 35),
3) with distorted grid voltage containing the fifth and seventh harmonics with 5% amplitudes of the fundamental (see Fig. 36).

Fig. 32 confirms filtering effectiveness by comparing phase currents in the *LCL* filter inductances. Under sinusoidal and symmetrical supply voltage, the control algorithm achieves a

Fig. 31. Laboratory setup view: (1) converter cabinet, (2) HMI, (3) signal panel, (4) oscilloscope, (5) power analyzer, (6) programming laptop, (7) AC–DC converter, (8) *LCL* filter inductance L_2, (9) *LCL* filter capacitance C, (10) *LCL* filter inductance L_1, (11) main control board with DSP and FPGA.

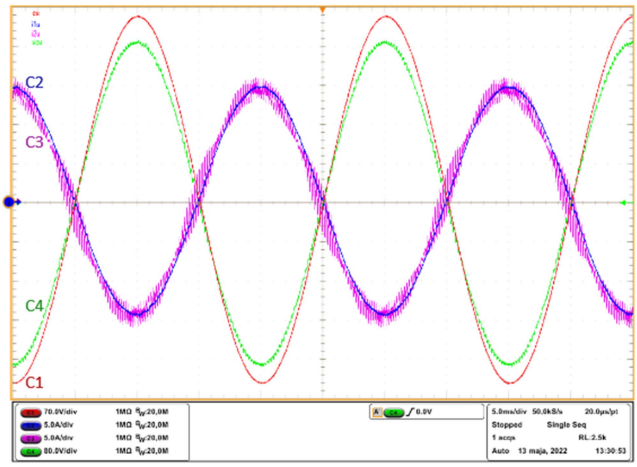

Fig. 32. Waveforms of the e_u (C1-red), i_{1u} (C2-blue), i_{2u} (C3-magenta), and u_{cu} (C4-green) during a step change in i^s_{1d} at $i^s_{1d} = -14.8$ A.

low THD of the generated grid current, ranging from 0.46% with $i^s_{1d} = 14.8$ A (see Fig. 33) to 3.43% with $i^s_{1d} = 2.1$ A (see Fig. 34). An abnormal power supply condition, with a halved amplitude of e_u, results in a THD increase to 0.60% (see Fig. 35). Despite distorted power supply voltage, the algorithm effectively suppresses disturbances, maintaining a satisfactory 2.80% THD for i_{1u} (see Fig. 36). Notably, low distortion is achieved with a modulator operating at a relatively low 5 kHz frequency.

The second research stage involves verifying the converter's response to a step change in the i^s_{1d}. Fig. 37 depicts the system response over a more extended observation period. Figs. 38 and 39 provides oscillograms with a shorter observation period for more precise insights into voltage and current changes in the converter system with an *LCL* filter.

Fig. 38 presents the regulation process after a step change in the i^s_{1d} from -7.5 A to -15 A. The forceful reduction of the i_{1d} results in increased oscillations in the voltage of the *LCL* filter capacitor, which diminish approximately 2.0 ms after the abrupt change in the i^s_{1d}. Nevertheless, the system maintains stability.

Comparison of Figs. 38 and 39 shows a different dynamic response. The regulation time is related to the length of available

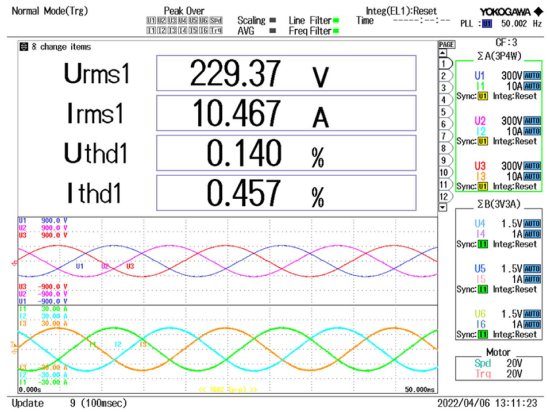

Fig. 33. Grid voltages e_u, e_v, e_w, and phase currents i_{1u}, i_{1v}, i_{1w} at $i^s_{1d} = 14.8$ A.

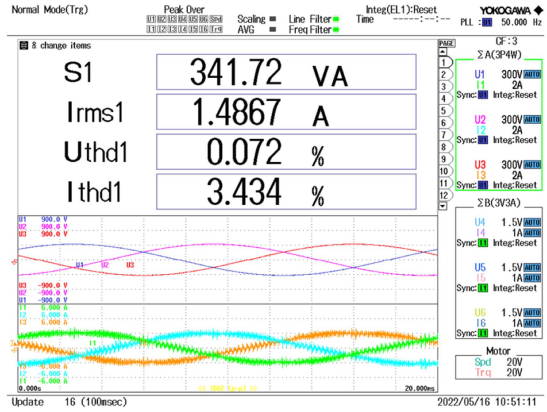

Fig. 34. Grid voltages e_u, e_v, e_w, and phase currents i_{1u}, i_{1v}, i_{1w} at $i^s_{1d} = 2.1$ A.

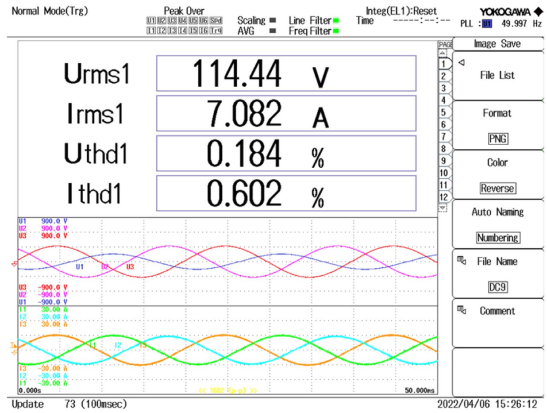

Fig. 35. Grid voltages e_u, e_v, e_w, and phase currents i_{1u}, i_{1v}, i_{1w} at $i^s_{1d} = 10.0$ A and asymmetric grid voltage, i.e., 0.5 E_u, E_v, E_w.

vectors of derivatives $\boldsymbol{d}_{2u}$. According to Fig. 5, vector 101 should be utilized to decrease the value in the d-axis of the $\boldsymbol{u}_{2dq}$, while vector 110 should be used to increase its value in the d-axis. Individual voltage vectors interact with the $\boldsymbol{i}_{2dq}$, as presented in Fig. 6. The derivatives of the current vector $\boldsymbol{d}_{2i}$ associated with vectors 101 and 110 are visible in the mentioned figure. Hence,

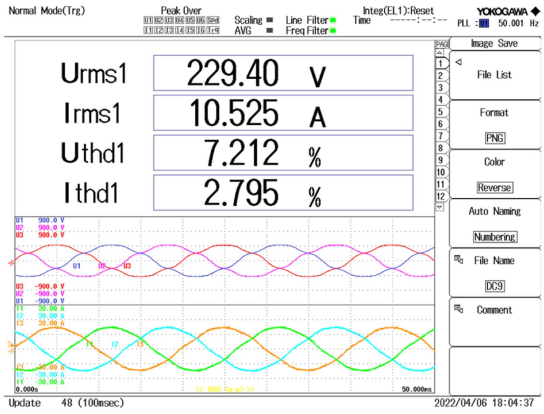

Fig. 36. Grid voltages e_u, e_v, e_w, and phase currents i_{1u}, i_{1v}, i_{1w} at $i_{1d}^s = 14.8$ A and distorted grid voltage by adding 5% of the fifth and seventh harmonics.

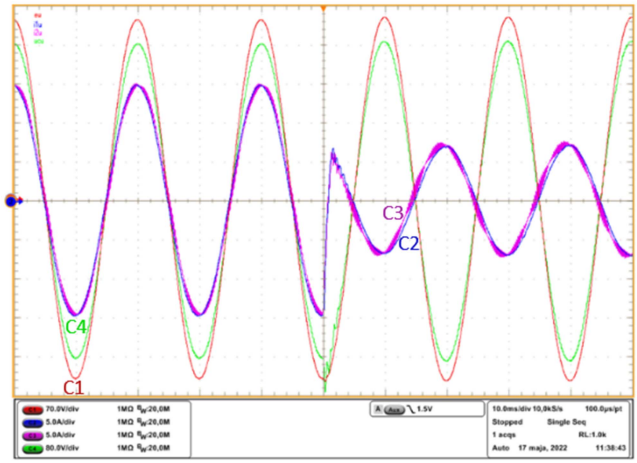

Fig. 37. Waveforms of the e_u (C1-red), i_{1u} (C2-blue), i_{2u} (C3-magenta), and u_{cu} (C4-green) during a step change in i_{1d}^s from $+15$ A to -7.5 A.

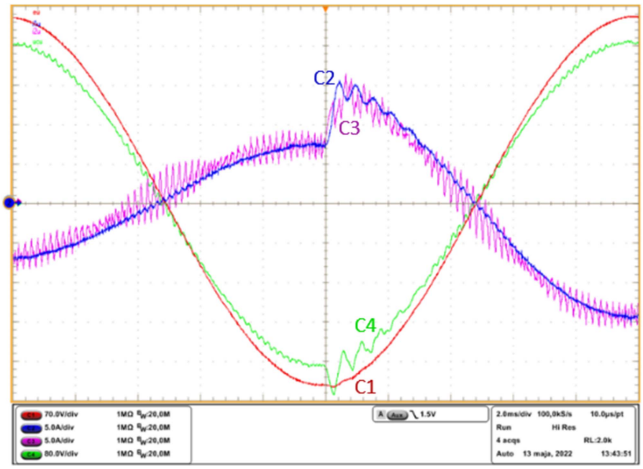

Fig. 38. Waveforms of the e_u (C1-red), i_{1u} (C2-blue), i_{2u} (C3-magenta), and u_{cu} (C4-green) during a step change in i_{1d}^s from -7.5 A to -15 A.

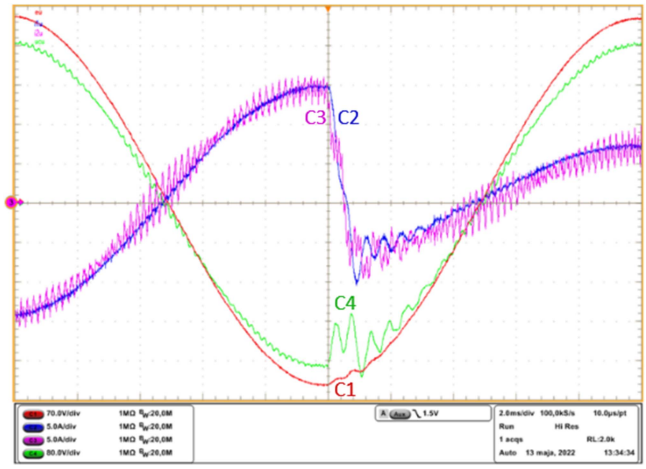

Fig. 39. Waveforms of the e_u (C1-red), i_{1u} (C2-blue), i_{2u} (C3-magenta), and u_{cu} (C4-green) during a step change in i_{1d}^s from -15 A to $+7.5$ A.

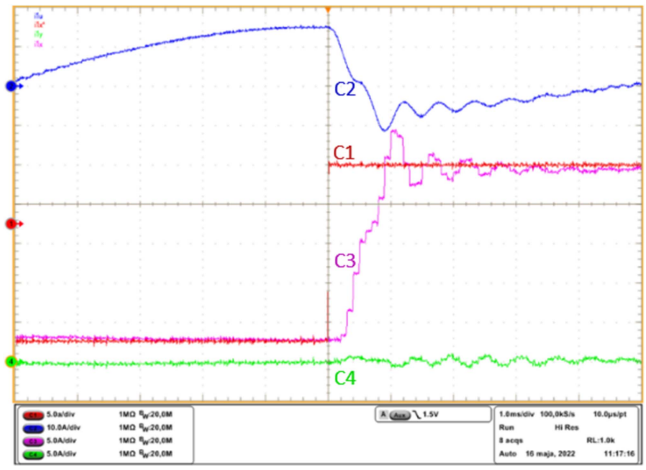

Fig. 40. Waveforms of the i_{1d}^s (C1-red), i_{1u} (C2-blue), i_{1d} (C3-magenta), and i_{1q} (C4-green) during a step change in i_{1d}^s from -15 A to $+7.5$ A.

it is known that applying vector 101 leads to faster changes in the i_{2dq}. It is important to note that changing only one component of the $\boldsymbol{i}_{2dq}$ is impossible. Activating any converter voltage vector results in a simultaneous change in both components.

Figs. 39 and 40 show how the regulation process works when the supply voltage is symmetrical and the i_{1d}^s changes from -15 A to $+7.5$ A. In Fig. 40, particular attention should be paid to the i_{1q} waveform. During the transient state, the algorithm selects converter voltage vectors so that the i_{1q} does not undergo significant changes (up to 0.6 A). It takes approximately 1.0 ms for the i_{1d} to reach the new set value after the change in the i_{1d}^s (see Fig. 40).

IX. Conclusion

The main objective of this work was to develop a new CCS C-BMPC to regulate a grid-connected ac–dc converter with an *LCL* input filter. The prediction mechanism in the developed

control method utilizes an optimization criterion, achieving compensation for the regulation error of the grid current vector in a single control period. Based on this criterion, the algorithm determines the switch-on times of individual voltage vectors used in modulation. The set of vectors chosen for modulation ensures minimal current THD in static state and stability during transient states, with relatively low switching frequency. Using the modulator results in a constant average switching frequency of the converter transistors, significantly facilitating the design of the coupling filter between the converter and the power grid. Current prediction does not require the application of complicated dead-time correction algorithms, causing current distortions during zero-crossings, especially at low current amplitudes. The developed method demonstrates high robustness to common disturbances in the power grid voltage, such as higher harmonics or asymmetry. Simulations and laboratory tests confirm the above advantages of the developed method.

REFERENCES

[1] A. Sikorski and M. Korzeniewski, "AC/DC/AC converter in a small hydroelectric power plant," *Bull. Polish Acad. Sci., Tech. Sci.*, vol. 59, no. 4, pp. 507–511, 2011, doi: 10.2478/v10175-011-0062-6.

[2] Y. Song, X. Wang, and F. Blaabjerg, "Doubly fed induction generator system resonance active damping through stator virtual impedance," *IEEE Trans. Ind. Electron.*, vol. 64, no. 1, pp. 125–137, Jan. 2017, doi: 10.1109/TIE.2016.2599141.

[3] R. Errouissi, M. Muyeen, A. Al-Durra, and S. Leng, "Experimental validation of a robust continuous nonlinear model predictive control based grid-interlinked photovoltaic inverter," *IEEE Trans. Ind. Electron.*, vol. 63, no. 7, pp. 4495–4505, Jul. 2016, doi: 10.1109/TIE.2015.2508920.

[4] N. Müller, S. Kouro, M. Malinowski, C. A. Rojas, M. Jasinski, and G. Estay, "Medium-voltage power converter interface for multigenerator Marine energy conversion systems," *IEEE Trans. Ind. Electron.*, vol. 64, no. 2, pp. 1061–1070, Feb. 2017, doi: 10.1109/TIE.2016.2615276.

[5] S. Vazquez, A. Marquez, R. Aguilera, D. Quevedo, J. I. Leon, and L. G. Franquelo, "Predictive optimal switching sequence direct power control for grid-connected power converters," *IEEE Trans. Ind. Electron.*, vol. 62, no. 4, pp. 2010–2020, Aug. 2015, doi: 10.1109/TIE.2014.2351378.

[6] S. Kwak, U.-C. Moon, and J.-C. Park, "Predictive-control-based direct power control with an adaptive parameter identification technique for improved AFE performance," *IEEE Trans. Power Electron.*, vol. 29, no. 11, pp. 6178–6187, Nov. 2014, doi: 10.1109/TPEL.2014.2298041.

[7] J. Scoltock, T. Geyer, and U. Madawala, "Model predictive direct current control for a grid-connected converter: LCL-filter versus L-filter," in *Proc. IEEE Int. Conf. Ind. Technol.*, Feb. 2013, pp. 576–581, doi: 10.1109/ICIT.2013.6505735.

[8] J. Dannehl, C. Wessels, and F. W. Fuchs, "Limitations of voltage-oriented PI current control of grid-connected PWM rectifiers with LCL filters," *IEEE Trans. Ind. Electron.*, vol. 56, no. 2, pp. 380–388, Feb. 2009, doi: 10.1109/TIE.2008.2008774.

[9] J. R. Rodriguez, J. W. Dixon, J. R. Espinoza, J. Pontt, and P. Lezana, "PWM regenerative rectifiers: State of the art," *IEEE Trans. Ind. Electron.*, vol. 52, no. 1, pp. 5–22, Feb. 2005, doi: 10.1109/TIE.2004.841149.

[10] Y. Tian i Q. Jiang, "A dual-current-loop control method based on system current detection for LCL-filter-based Active Power filters," in *Proc. 39th Annu. Conf. IEEE Ind. Electron. Soc.*, Nov. 2013, pp. 8498–8503, doi: 10.1109/IECON.2013.6700559.

[11] A. A. Nazeri, P. Zacharias, F. M. Ibanez, and S. Somkun, "Design of proportional-resonant controller with zero steady-State error for a single-phase grid-connected voltage source inverter with an LCL output filter," in *Proc. IEEE Milan PowerTech*, Jun. 2019, pp. 1–6, doi: 10.1109/PTC.2019.8810554.

[12] M. Malinowski, M. Jasinski, and M. P. Kazmierkowski, "Simple direct power control of three-phase PWM rectifier using space-vector modulation (DPC-SVM)," *IEEE Trans. Ind. Electron.*, vol. 51, no. 2, pp. 447–454, Apr. 2004, doi: 10.1109/TIE.2004.825278.

[13] S. Vazquez, J. Rodriguez, M. Rivera, L. G. Franquelo, and M. Norambuena, "Model predictive control for power converters and drives: Advances and trends," *IEEE Trans. Ind. Electron.*, vol. 64, no. 2, pp. 935–947, Feb. 2017, doi: 10.1109/TIE.2016.2625238.

[14] S. Kouro, M. A. Perez, J. Rodriguez, A. M. Llor, and H. A. Young, "Model predictive control: MPC's role in the evolution of power electronics," *IEEE Ind. Electron. Mag.*, vol. 9, no. 4, pp. 8–21, Dec. 2015, doi: 10.1109/MIE.2015.2478920.

[15] A. Bouafia, J.-P. Gaubert, and F. Krim, "Predictive direct power control of three-phase pulsewidth modulation (PWM) rectifier using space-vector modulation (SVM)," *IEEE Trans. Power Electron.*, vol. 25, no. 1, pp. 228–236, Jan. 2010, doi: 10.1109/TPEL.2009.2028731.

[16] A. Sikorski i R. Grodzki, "Predictive control of the AC/DC converter," in *Proc. 16th Int. Power Electron. Motion Control Conf. Expo.*, Oct. 2014, pp. 131–136, doi: 10.1109/EPEPEMC.2014.6980682.

[17] Z. Song, Y. Tian, W. Chen, Z. Zou, and Z. Chen, "Predictive duty cycle control of three-phase active-front-end rectifiers," *IEEE Trans. Power Electron.*, vol. 31, no. 1, pp. 698–710, Jan. 2016, doi: 10.1109/TPEL.2015.2398872.

[18] Š. Ileš, T. Bariša, D. Sumina, and J. Matuško, "Hybrid CCS/FCS model predictive current control of a grid connected two-level converter," in *Proc. IEEE 18th Int. Power Electron. Motion Control Conf.*, Aug. 2018, pp. 981–986, doi: 10.1109/EPEPEMC.2018.8521996.

[19] B. Liu, T. Chen, and W. Song, "The essential relationship between deadbeat predictive control and continuous-control-set model predictive control for PWM converters," in *Proc. Int. Power Electron. Conf.*, May 2018, pp. 1872–1876, doi: 10.23919/IPEC.2018.8508017.

[20] C. Xue, D. Zhou, and Y. Li, "Hybrid model predictive current and voltage control for LCL-filtered grid-connected inverter," *IEEE J. Emerg. Sel. Topics Power Electron.*, vol. 9, no. 5, pp. 5747–5760, Oct. 2021, doi: 10.1109/JESTPE.2020.3049083.

[21] P. Falkowski and A. Sikorski, "Finite control set model predictive control for grid-connected AC–DC converters with LCL filter," *IEEE Trans. Ind. Electron.*, vol. 65, no. 4, pp. 2844–2852, Apr. 2018, doi: 10.1109/TIE.2017.2750627.

[22] C. Cheng, H. Nian, X. Wang, and D. Sun, "Dead-beat predictive direct power control of voltage source inverters with optimised switching patterns," *IET Power Electron.*, vol. 10, no. 12, pp. 1438–1451, 2017, doi: 10.1049/iet-pel.2016.0869.

[23] Y. Yang et al., "A novel continuous control set model predictive control for *LC* -filtered three-phase four-wire three-level voltage-source inverter," *IEEE Trans. Power Electron.*, vol. 38, no. 4, pp. 4572–4584, Apr. 2023, doi: 10.1109/TPEL.2023.3233995.

[24] H. Zamani, K. Abbaszadeh, M. H. Karimi, and J. Gyselinck, "Adaptive model predictive control for *LCL* -filter grid-tied inverters," *IEEE Trans. Ind. Electron.*, vol. 71, no. 8, pp. 8903–8914, Aug. 2024, doi: 10.1109/TIE.2023.3325574.

[25] K. S. Alam, M.. P. Akter, D. Xiao, D. Zhang, and M. F. Rahman, "Asymptotically stable predictive control of grid-connected converter based on discrete space vector modulation," *IEEE Trans. Ind. Inform.*, vol. 15, no. 5, pp. 2775–2785, May 2019, doi: 10.1109/TII.2018.2876274.

[26] M. Abdelrahem, F. Hamadto, A. Garikapati, R. Kennel, and J. Rodríguez, "Multiple-vector direct model predictive control for grid-connected power converters with reduced calculation burden," in *Proc. IEEE Int. Symp. Predictive Control Elect. Drives Power Electron.*, May 2019, pp. 1–6, doi: 10.1109/PRECEDE.2019.8753253.

[27] H.-C. Moon, J.-S. Lee, and K.-B. Lee, "A robust deadbeat finite set model predictive current control based on discrete space vector modulation for a grid-connected voltage source inverter," *IEEE Trans. Energy Convers.*, vol. 33, no. 4, pp. 1719–1728, Dec. 2018, doi: 10.1109/TEC.2018.2830776.

[28] P. Falkowski, A. Sikorski, and M. Malinowski, "Finite control set model predictive control with floating virtual voltage vectors for grid-connected voltage source converter," *IEEE Trans. Power Electron.*, vol. 36, no. 10, pp. 11875–11885, Oct. 2021, doi: 10.1109/TPEL.2021.3067602.

[29] T. Geyer, P. Karamanakos, and R. Kennel, "On the benefit of long-horizon direct model predictive control for drives with LC filters," in *Proc. IEEE Energy Convers. Congr. Expo.*, Pittsburgh, PA, USA: IEEE, Sep. 2014, pp. 3520–3527, doi: 10.1109/ECCE.2014.6953879.

[30] T. Geyer i D. E. Quevedo, "Performance of Multistep finite control set model predictive control for power electronics," *IEEE Trans. Power Electron.*, vol. 30, no. 3, pp. 1633–1644, Mar. 2015, doi: 10.1109/TPEL.2014.2316173.

[31] R. Teodorescu, F. Blaabjerg, M. Liserre, and P. C. Loh, "Proportional-resonant controllers and filters for grid-connected voltage-source converters," *IEE Proc., Electr. Power Appl.*, vol. 153, no. 5, 2006, Art. no. 750, doi: 10.1049/ip-epa:20060008.

[32] J. Dannehl, F. W. Fuchs, S. Hansen, and P. B. Thøgersen, "Investigation of active damping approaches for PI-based current control of grid-connected pulse width modulation converters with LCL filters," *IEEE Trans. Ind. Appl.*, vol. 46, no. 4, pp. 1509–1517, Jul./Aug. 2010, doi: 10.1109/TIA.2010.2049974.

[33] S. Golestan, J. M. Guerrero, J. C. Vasquez, A. M. Abusorrah, V. Khadkikar, and J. Rodriguez, "Control design of grid synchronization systems for grid-tied power converters using symmetrical optimum method: A comprehensive reference," *IEEE Trans. Power Electron.*, vol. 38, no. 11, pp. 13650–13673, Nov. 2023, doi: 10.1109/TPEL.2023.3292306.

[34] Z. Zhao, Z. Sun, Y. Feng, B. Ji, S. Wang, and J. Zhao, "High-performance resonant controller implemented in the discrete-time domain for voltage regulation of grid-forming converters," *IEEE Trans. Power Electron.*, vol. 37, no. 4, pp. 3913–3926, Apr. 2022, doi: 10.1109/TPEL.2021.3120426.

Krzysztof Dmitruk received the M.Sc. and Ph.D. degrees in electrical engineering from the Bialystok University of Technology, Bialystok, Poland, 2016 and 2023, respectively.

Since 2017, he has been an Assistant Professor with Bialystok University of Technology. His research interests include the interaction of power electronic converters with electrical grids, renewable energy sources, and energy storage systems.

Dr. Dmitruk was a key researcher in two prestigious grants funded by the Polish National Centre for Research and Development, which focused on designing and developing prototype power electronic devices for aircraft power supply systems.

Andrzej Sikorski received the M.Sc. degree from Bialystok University of Technology, Bialystok, Poland, in 1980, the Ph.D. degree from Warsaw University of Technology, Warsaw, Poland, in 1989, and the D.Sc. degree from Poznan University of Technology, Poznan, Poland, in 2000, all in electrical engineering.

He has authored and coauthored more than 150 papers in technical journals and conference proceedings. He was bestowed a professorship in technical sciences by the President of the Republic of Poland. His research interests include the areas of electric drives and power electronics, particularly ac/dc/ac, matrix converters, and their control.